

Department of Physics and Astronomy
University of Heidelberg

Bachelor Thesis in Physics
submitted by

Alexander Koch

born in Düren (Germany)

2015

Eta meson production with conversions in ALICE in pp collisions at $\sqrt{s} = 2.76$ TeV and $\sqrt{s} = 8$ TeV

This Bachelor Thesis has been carried out by Alexander Koch at the
Physikalisches Institut at the University of Heidelberg
under the supervision of
PD Dr. Klaus Reygers

Abstract

The η meson production in pp collisions with a center of mass energy of $\sqrt{s}=2.76$ TeV and 8 TeV is studied with the Photon Conversion Method (PCM) at the ALICE experiment at LHC. This method exploits the ALICE Inner Tracking System (ITS) and the Time Projection Chamber (TPC) to reconstruct photons which convert in the detector material. With the minimum bias data recorded in the 2011 pp run at $\sqrt{s}=2.76$ TeV and in the 2012 pp run at $\sqrt{s}=8$ TeV, it will be possible to measure the differential invariant cross section of the η meson as function of the transverse momentum and extract the η/π^0 ratio.

The analyzed transverse momentum range for the data recorded at 2.76 TeV reaches from 0.5 GeV/ c to 6 GeV/ c and for 8 TeV from 0.4 GeV/ c to 8 GeV/ c . In addition the results of the η meson analysis will be compared to NLO pQCD calculations.

Zusammenfassung

Die η Mesonen Produktion in pp Kollisionen mit einer Schwerpunktsenergie von $\sqrt{s}=2.76$ TeV und 8 TeV wird mit der Photon Conversion Method (PCM) am ALICE Experiment des LHCs untersucht. Dieses Verfahren nutzt das ALICE Inner Tracking System (ITS) und die Time Projection Chamber (TPC), um Photonen die im Detektormaterial konvertieren zu rekonstruieren. Mit den Minimum Bias pp Daten von 2011, bei einer Schwerpunktsenergie von $\sqrt{s}=2.76$ TeV, und von 2012, bei $\sqrt{s}=8$ TeV, wird es möglich sein den differentiellen invarianten Wirkungsquerschnitt des η Mesons als Funktion des transversen Impulses zu extrahieren, sowie das Verhältnis η/π^0 zu bestimmen.

Der analysierte Transversalimpulsbereich bei 2.76 TeV erstreckt sich von 0.5 GeV/ c bis 6 GeV/ c und bei 8 TeV von 0.4 GeV/ c bis 8 GeV/ c . Abschließend werden die Ergebnisse der η Meson Analyse mit NLO pQCD Berechnungen verglichen.

Contents

1	Motivation	3
2	Theoretical Background	3
2.1	Fundamental Interactions and the Standard Model	3
2.2	Quark-Gluon Plasma	4
2.3	η meson	5
2.4	Photon and Electron interaction with matter	6
3	Experimental Setup	9
3.1	Large Hadron Collider	9
3.2	ALICE Detector	10
3.3	Trigger	14
3.4	Software	14
4	Datasets and Photon Reconstruction	15
4.1	Datasets and Event Selection	15
4.1.1	Monte Carlo Simulations	16
4.2	Photon Reconstruction	18
4.2.1	Track and V^0 Selection	18
4.2.2	Electron Selection	19
4.2.3	Photon Selection	20
5	η Meson Analysis	24
5.1	Meson Reconstruction	24
5.1.1	Meson Signal Extraction	25
5.2	Spectra Corrections	26
5.2.1	Secondary Pions Correction	26
5.2.2	Out of the Bunch Pile Up Correction	27
5.2.3	Corrections for Acceptance and Efficiency	30
5.2.4	Correction for finite bin width	32
5.2.5	Systematic Error Evaluation	32
5.3	Corrected Spectra and Comparison to Theory	35
5.4	η/π^0 Ratio	38
6	Conclusion and Outlook	38
7	Appendix	39
7.1	Analyzed Runs	39
7.2	Electron Selection	41
7.3	Photon Selection	41
7.4	Signal Extraction	42
7.5	DCA Bins	46
7.6	Added Signals Weighting	48
7.7	Systematic Error	49
8	Acronyms and Technical Terms	53

1 Motivation

At the moment the most powerful particle accelerator is the Large Hadron Collider (LHC) at the European Organization for Nuclear Research (CERN). There Proton-Proton, Proton-Lead and Lead-Lead collisions are studied at high energies, allowing a deep look into matter.

Understanding the η meson production in Proton-Proton (pp) collisions could improve the knowledge about the η mesons fragmentation function. Furthermore the measurement of η mesons is also used as a reference measurement in heavy ion collisions. In heavy ion collisions the creation of a Quark-Gluon Plasma (QGP) is expected. The QGP is the state of matter which is thought to be dominating shortly after the Big Bang.

As one of the four major experiments at the LHC the A Large Ion Collider Experiment (ALICE) reveals the fundamental bricks of matter and helps understanding the state of the early universe.

2 Theoretical Background

2.1 Fundamental Interactions and the Standard Model

The Standard Model (SM) describes the electromagnetic interaction, the weak interaction and the strong interaction between particles through the exchange of gauge bosons. These are three of the four known fundamental interactions, as gravity is not explained by this model. The particles which experience the fundamental interactions are divided into three generations and consist of gauge bosons and fermions, which are subdivided into leptons and quarks.

Figure 1 shows an overview of the particles of the standard model. Fermions are the fundamental bricks of all known matter in the universe.

Leptons do not experience the strong interaction but the electromagnetic and weak interaction. Since there is no evidence of an internal structure smaller than $<10^{-18}$ m leptons are considered as point like particles.[31] They come in six different flavors which are electrons e , muons μ and tauons τ with their respective neutrinos. The neutrinos mass is close to zero and as they do not have an electrical charge they only participate in the weak interaction.

W^\pm and Z^0 bosons are carrier particles for the weak force while photons are the carrier particles for the electromagnetic force. The electromagnetic interaction and the weak interaction are described by the electroweak theory.

Quarks also consist of six flavors and experience the strong interaction by the exchange of eight gluons g . The quarks are considered to carry a color charge which can adopt three different colors (e.g. red, green, blue). Due to the rules of the strong interaction quarks try to form a color neutral particle which are called hadrons. Color neutral hadrons can be achieved by combining all three colors or combining a color with its anti-color. As quarks can only be observed in color neutral particles, it is not possible to observe single quarks and therefore colors. This principle is referred to as confinement.

Particles that consist of three quarks are called baryons. On the other hand mesons are build of a quark-antiquark pair, which carry a color and the corresponding anti-color. Moreover the 8 gluons also carry a color and an anti-color and are thus able to change

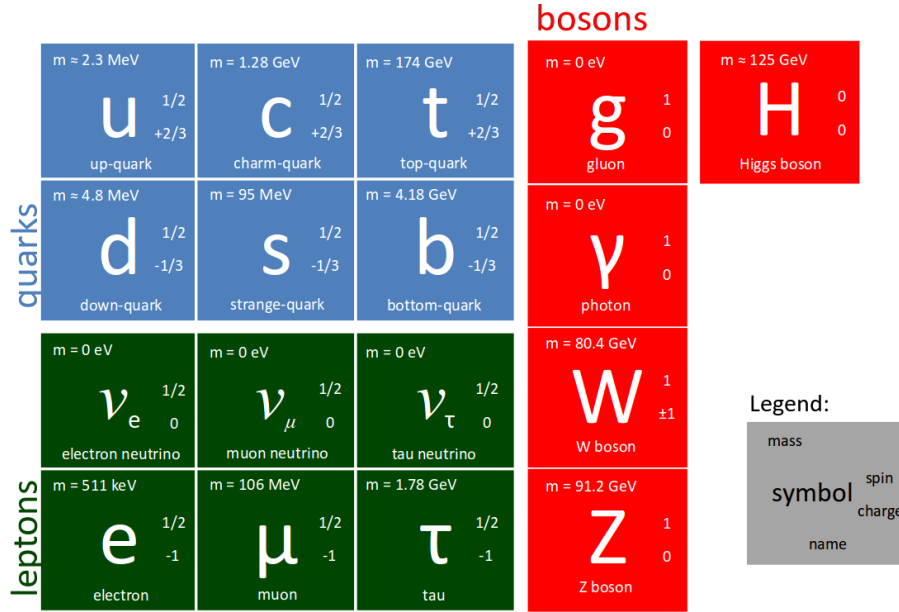


Figure 1: Fundamental particles of the standard model [25] [30]

the color of the quark content of hadrons.[23]

The color charge of gluons and quarks can be seen as the 'charge of the strong interaction'.

2.2 Quark-Gluon Plasma

The idea of asymptotic freedom describes the increasing coupling strength between quarks for larger distances and decreasing coupling strength for smaller distances. This leads to the idea of free quarks and gluons at high energies and densities. To overcome the boundary of confinement it needs critical temperatures T_c of about 150-200 MeV [11]. There the hadrons release their quark and gluon content and form a new state of matter which is called Quark-Gluon Plasma (QGP).

In order to study this state of matter heavy ion collisions with a large number of colliding nucleons are needed to form a QGP. When the collision takes place the critical temperature is passed and the boundaries of confinement disappear. This allows free quarks and gluons to form a local equilibrium for a short lapse of time. The fireball coming from the collision will expand and therefore cool down. When it reaches the critical temperature T_c the hadronic freeze out will begin and the quarks and gluons form hadronic matter again. The Quantum Chromodynamics (QCD) phase diagram in Figure 2 shows the boundary between the hadronic matter and the QGP in dependence of the temperature T and the baryon chemical potential μ_B .

It is thought that in the early universe about 10 ps to 10 ms after the big bang the Quark-Gluon Plasma (QGP) was the dominating state of matter.[14] For high densities which are most likely reached in neutron stars an even more exotic state of matter with color superconductivity is expected.

To study the characteristics of the QGP several experiments worldwide are carried out. The experiments at Alternating Gradient Synchrotron (AGS), Super Proton Synchrotron (SPS), Relativistic Heavy Ion Collider (RHIC) and LHC to name a few are all studying

the evolution of matter in the QCD phase diagram.

Creating a QGP usually needs a large number of nucleons colliding to achieve high densities and energies such as in Au-Au collisions at RHIC or Pb-Pb collisions at LHC. Therefore proton proton collisions are not expected to form a QGP as seen in heavy ion collisions. It might be possible that in high multiplicity pp collisions a mini-QGP with a thermalization time $\tau_0 < 0.5$ fm and a size of approximately 2-3 fm can be formed.[34]

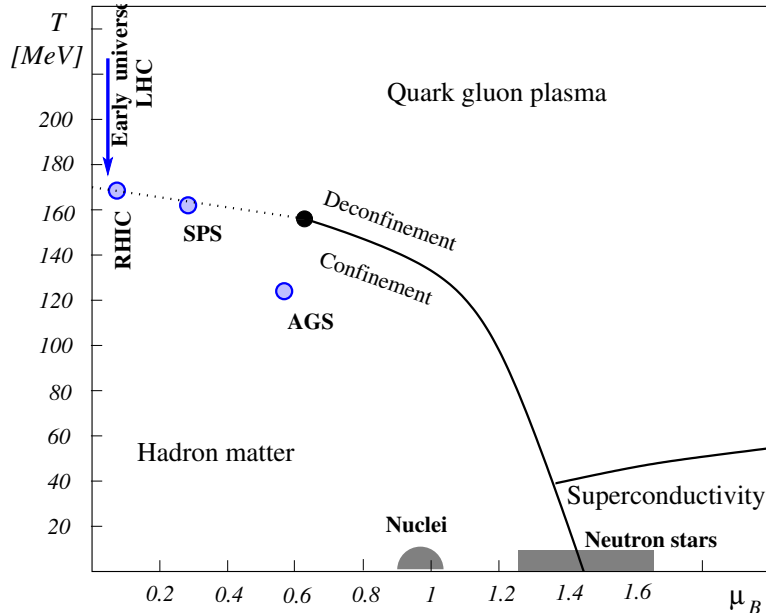


Figure 2: Phase diagram of QCD in $T - \mu_B$ plane. [21]

2.3 η meson

The quark content of the η meson is a superposition of three quantum states $|\eta\rangle = \frac{1}{\sqrt{6}} \cdot (|u\bar{u}\rangle + |d\bar{d}\rangle - 2|s\bar{s}\rangle)$ with an invariant mass of $m_\eta = (547.862 \pm 0.018) \text{ MeV}/c^2$. [26] As the η meson is not stable it decays with a probability of about 72.12% into neutral daughter particles and with a probability of 28.1% to charged particles which mainly consist of charged pions. In Table 1 the branching ratios (BR) for the main η meson decays are shown. This analysis uses the Photon Conversion Method (PCM) to detect the η mesons electromagnetic decay in two photons with a BR of 39.41% in order to extract the η meson yield.

Decay modes	BR
2γ	$(39.41 \pm 0.20)\%$
$3\pi^0$	$(32.68 \pm 0.23)\%$
$\pi^+\pi^-\pi^0$	$(22.92 \pm 0.28)\%$
$\pi^+\pi^-\gamma$	$(4.22 \pm 0.08)\%$
$e^+e^-\gamma$	$(0.69 \pm 0.04)\%$

Table 1: branching ratio (BR) of the main η meson decay modes [26]

2.4 Photon and Electron interaction with matter

To measure the η meson with the PCM the two photons coming from the mesons decay have to be detected. Therefore it is substantial to understand the interactions of photons with matter at different energies. As shown in Figure 3 there are three main ways photons can interact with matter: photoelectric effect for low energies, compton scattering which dominates at approximately 1 MeV and pair production which dominates for high energies.

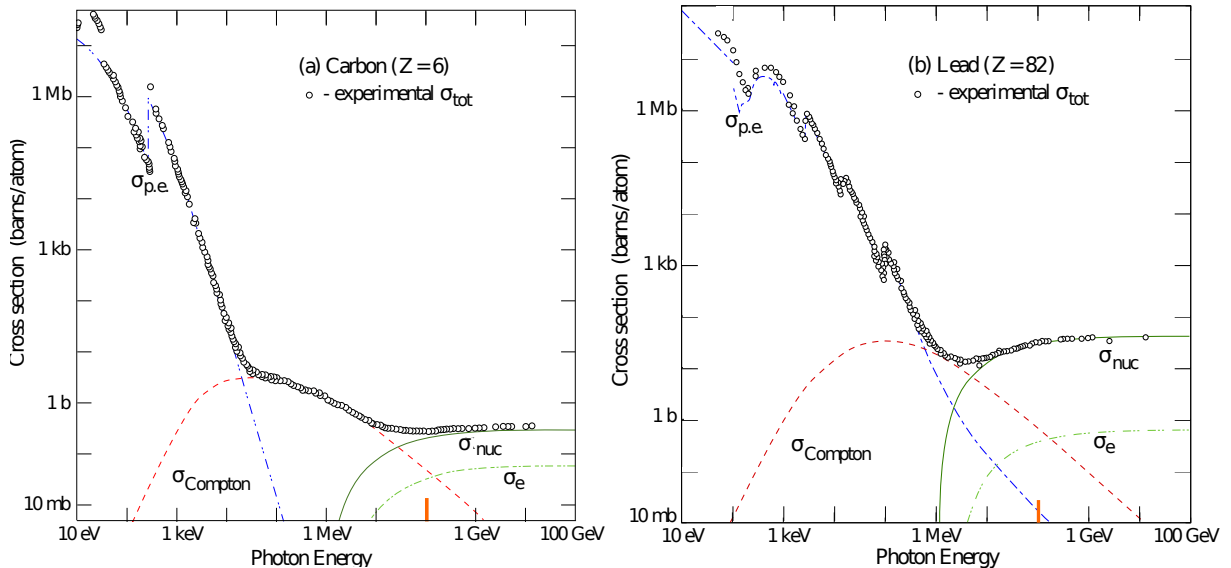


Figure 3: Total cross section of photons in carbon(left) and in lead(right) as function of the energy. The different cross section contributions to the total measured cross section (open circles) are shown.[26] $\sigma_{p.e.}$: photoelectric effect, $\sigma_{Compton}$: compton effect, σ_{nuc} : pair production in nuclear field and σ_e : pair production in electron field

Photoelectric Effect

The photoelectric effect occurs when a photon is absorbed by an electron and ionizes the atom. Therefore a minimum energy is necessary for the photon. The photons minimum energy depends on the binding energy E_b of the material. Typically this energy is of the order of ~ 10 eV for most elements. If the photons energy E_γ is bigger than the binding energy E_b , the photoelectric effect can take place and an electron with the kinetic energy $E_{kin,e}$ is released from the material:

$$E_{kin,e} = E_\gamma - E_b \quad (1)$$

The cross section for the photoelectric effect rules the total photon cross section at low energies and decreases quickly, depending on the material.

Compton Scattering

In a range of approximately 100 keV up to 10 MeV compton scattering dominates the total photon cross section. If compton scattering happens a photon with the wavelength λ scatters inelastic at an electron and an energy transfer from the photon to the electron

will occur. The scattered photon loses energy depending on the angle θ and has therefore a longer wavelength λ' .

$$\lambda' - \lambda = \frac{h}{m_e c} (1 - \cos \theta) \quad (2)$$

Photon Conversion

If the photon's energy reaches approximately the mass $m_{e^-e^+} = 1.022 \text{ MeV}/c^2$, which is equivalent to the mass of an electron and a positron, it can interact with the Coulomb field of a nucleus and create an electron - positron pair. It is also possible, for a photon with the mass of $m_{e^-e^+}$, to create an electron - positron pair in the Coulomb field of an electron, but it is less likely than in a Coulomb field of a nucleus. According to [24] the cross section for pair production for large energies can be approximated by:

$$\sigma_{pair} \approx \frac{7}{9} \cdot \frac{A}{N_A} \cdot \frac{1}{X_0} \quad (3)$$

The value X_0 represents the radiation length in the material, N_A the Avogadro constant and A the atomic number. As the contributions of the photoelectric effect and the Compton scattering to the total photon cross section decrease to zero for high energies the total cross section above $\sim 10 \text{ MeV}$ is dominated by pair production.

Due to the high energies achieved in proton-proton collisions at LHC the main interaction of photons with the detector material is ruled by pair creation. The electrons and positrons themselves have a high energy and interact with the detector material.

For particle identification (PID) it is useful to know how the energy loss of electrons (positrons) can be described. Here ionization processes and the radiation of bremsstrahlung are the two main reasons for the energy loss of the electron. The energy loss of electrons due to ionization processes can be described by approximation using a modified Bethe-Bloch formula[24]:

$$-\frac{dE}{dx} = 4\pi N_A r_e^2 m_e c^2 \frac{Z}{A} \cdot \frac{1}{\beta^2} \left(\ln \frac{\gamma m_e c^2}{2I} - \beta^2 - \frac{\delta}{2} \right) \quad (4)$$

where,

- r_e is the electron radius
 - m_e the mass of the electron
 - β is speed of the incident particle v divided by the speed of light c
 - γ stands for the Lorentz factor which is defined as $\gamma = \frac{1}{\sqrt{1 - (\frac{v}{c})^2}}$
 - Z, A represent the atomic number and weight of the absorber
 - I stands for the mean excitation energy which is dependent on the molecular state and the atomic number Z
 - δ counts for the screening effects of the electric field
- A more detailed description of this parameter can be found in [24]

While the energy loss through excitation and ionization can be described by the modified Bethe-Bloch formula, the energy loss of electrons and positrons due to bremsstrahlung

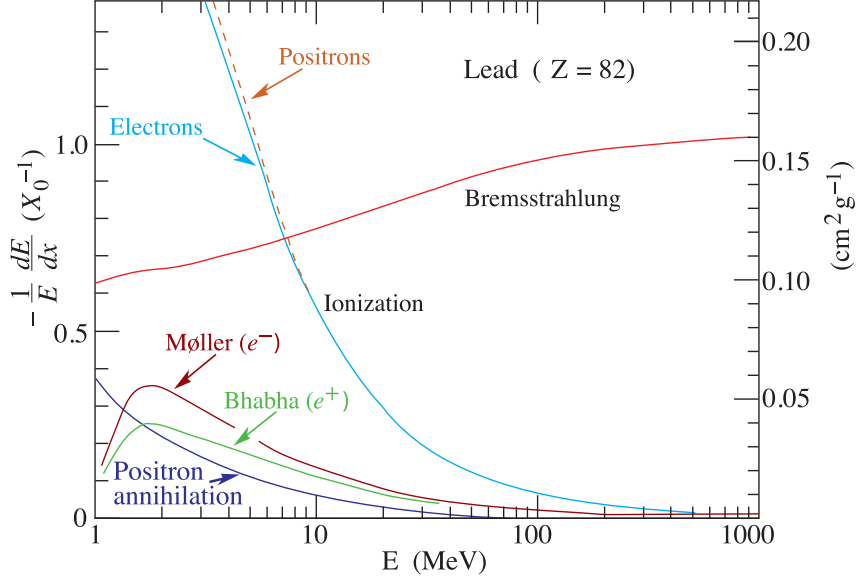


Figure 4: Energy loss of electrons and positrons in lead per radiation length X_0 [26]

can not be neglected. For high energies $E \gg m_e c^2 / \alpha Z^{1/3}$ the energy loss for electrons through bremsstrahlung can be approximated by[24]:

$$-\frac{dE}{dx} \approx \frac{E}{X_0} \approx 4\alpha N_a \cdot \frac{Z^2}{A} r_e^2 \cdot E \ln \frac{183}{Z^{1/3}} \quad (5)$$

The different contributions for the energy loss for electrons and positrons in lead can be seen in Figure 4. For energies above ~ 10 MeV bremsstrahlung becomes dominant. For small energies other process as Møller/Bhabba scattering and positron annihilation have a share at the total energy loss of electrons and positrons.

3 Experimental Setup

The European Organization for Nuclear Research (CERN) is a research facility located near Geneva at the border between Switzerland and France. Founded in 1954 its main purpose is exploring the fundamental particles and their interactions. As one of the first european joint-venture research projects there are now 21 countries participating at CERN, which runs the world wide largest particle accelerator the LHC.

3.1 Large Hadron Collider

In 2008 CERN started the Large Hadron Collider (LHC). The LHC has a circumference of about 27km, is located about 100 meter under the ground and it provides its 4 major experiments with high energy collisions at the 4 interaction points. There are three collision systems at the LHC: heavy-ion collisions (AA), proton-proton collisions (pp) and proton heavy-ion collisions (pA).

The LHC is designed for a maximum energy of $\sqrt{s} = 14$ TeV, a peak luminosity of $L = 10^{34} cm^{-2}s^{-1}$ in proton-proton (pp) collisions and maximum energy of $\sqrt{s_{NN}} = 5.52$ TeV in heavy-ion collisions (AA).

Four major experiments are carried out at the LHC: A Toroidal LHC Apparatus (ATLAS), LHC beauty (LHCb) experiment, Compact Muon Solenoid (CMS) experiment and A Large Ion Collider Experiment (ALICE). Their locations at the LHC are shown in Figure 5.

Exploring different physical characteristics, each of those experiments is equipped with its unique detectors and is located at one of the four LHC's interaction points.

- A Toroidal LHC Apparatus (ATLAS)
Probing for substructures of elementary particles and the discovery of new elementary particles is the motivation of ATLAS. In 2012 the ATLAS Collaboration announced the discovery of a new elementary particle in the energy range of the assumed Higgs boson.[1]
- Compact Muon Solenoid (CMS)
The CMS detector covers a large field of physics from the study of the Standard Model (SM), search for extra dimensions and for particles which could make up dark matter. The goals of CMS are very similar to those of the ATLAS detector. The CMS collaboration was also involved in the discovery of the Higgs boson.[16]
- LHC beauty (LHCb)
The LHCb detector is specialized on measuring hadronic decays containing a charm or bottom(beauty) quark. Precise measurements of CP-Violations or decays of rare particles test the Standard Model (SM).
- A Large Ion Collider Experiment (ALICE)
Investigating the QGP created in Pb-Pb collisions is the main purpose of the ALICE experiment. In the following section the ALICE detector is described more in detail.

In order to execute the LHC experiments both of the LHC's beampipes are filled with protons or lead ions which are then accelerated to the desired collision energy.

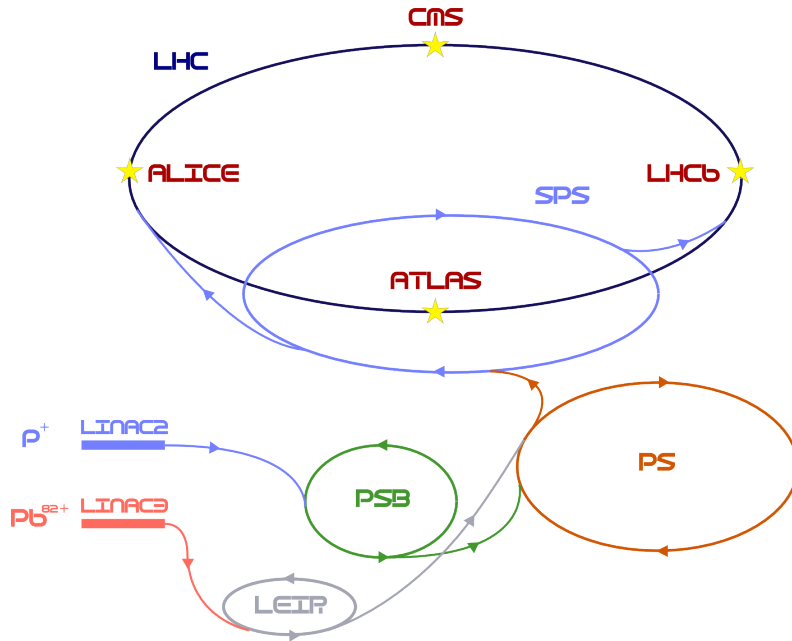


Figure 5: LHC injection scheme with preaccelerators and experiment overview. Reproduced from [15]

Before protons are injected in the LHC they are accelerated to an energy of 450 GeV. This is done by one linear accelerator and three circular accelerators which increase the protons energy step by step. A bottle of hydrogen gas in conjunction with an electric field creates a proton source. First the protons are accelerated by a linear accelerator (LINAC2) to an energy of 50 MeV. Then the protons are then injected into the Proton Synchrotron Booster (PSB) which they leave with an energy of 1.4 GeV. After the protons are accelerated in the PSB they are injected into the Proton Synchrotron (PS) reaching a maximum energy of 25 GeV. The last preaccelerator is the Super Proton Synchrotron (SPS) where the protons energy is increased up to 450 GeV. From the SPS the protons are injected with contrary direction of rotation in the two beam pipes of the LHC. There they are accelerated to their final collision energy.

Lead ions also are accelerated before entering the LHC. They come from the linear accelerator (LINAC3), passing the Low Energy Ion Ring (LEIR) and are filled into the Proton Synchrotron (PS) from where on they take the same path as the protons.[15]

The injection scheme for protons and lead ions is illustrated in figure 5.

3.2 ALICE Detector

The ALICE detector was designed to study the QGP, which is created in high energy heavy ion collisions. The detector has an overall weight of ≈ 10.000 t and measures about $26\text{ m} \times 26\text{ m} \times 16\text{ m}$. [15]

Inside the L3 solenoid magnet, which creates a magnetic field of $B = 0.5\text{ T}$ the central-barrel detectors are embedded. A cross section of the central-barrel detectors in 2012 is shown in Figure 7 and an overview of the whole ALICE setup in Figure 6. The Inner Tracking System (ITS) is placed directly around the beampipe and covers the full azimuthal range. It consist of two Silicon Pixel Detectors (SPD), two Silicon Drift Detec-

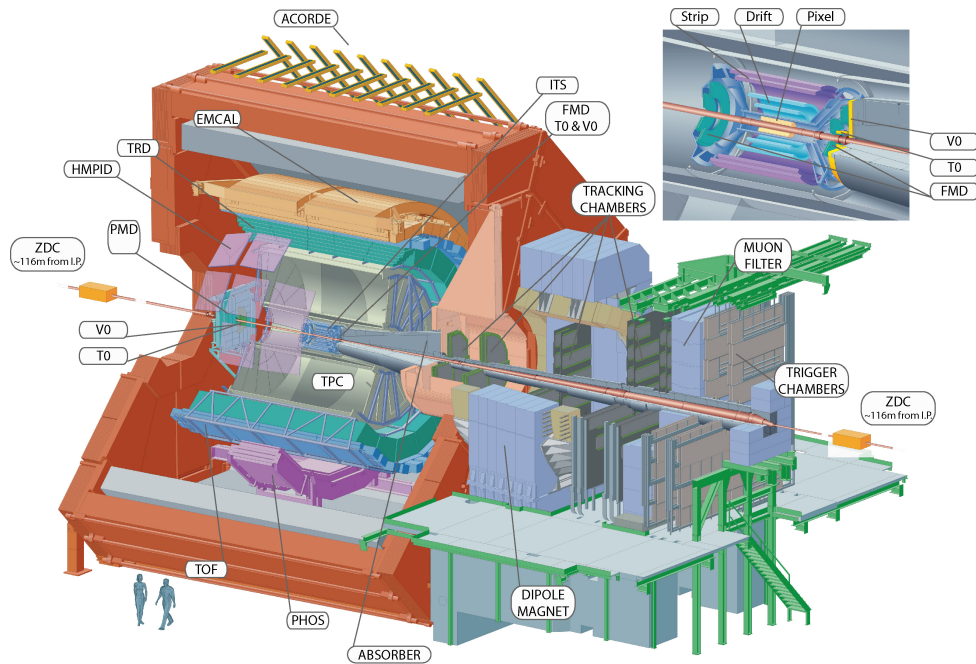


Figure 6: Overview of the ALICE detectors.[7]

tors (SDD) and two Silicon Strip Detectors (SSD) making up six tracking layers. Together with the ITS the Time Projection Chamber (TPC), which is located around the ITS, is one of the main tracking detectors for charged particles. Furthermore the Silicon Drift Detector (SDD) and TPC measure the specific energy loss (dE/dx) due to ionization of charged particles in order to identify them. The Transition Radiation Detector (TRD) is used for charged particle tracking and it helps identifying electrons by transition radiation and dE/dx measurements. The position of the Time-Of-Flight detector (TOF) is next to the TRD and it is the outermost central barrel detector which covers the whole azimuthal range. The other three detectors are the Photon Spectrometer (PHOS), the Electromagnetic Calorimeter (EMCal) and the High Momentum Particle Identification Detector (HMPID) which are located outside TOF but inside the L3 solenoid magnet. Detailed information of the position and acceptance of the central barrel detectors can be found in Table 2 and Figure 7. Each of the central barrel detectors is divided into 18 azimuthal parts covering an equal region of 20° . The detectors ITS, TPC, TRD* and TOF cover the full azimuthal range.

- Inner Tracking System (ITS)

The ITS covers the full azimuthal acceptance and a pseudorapidity range of $|\eta| < 0.9$. [3] It consists of six tracking layers which are divided into two Silicon Pixel Detectors (SPD), two Silicon Drift Detectors (SDD) and two Silicon Strip Detectors (SSD). Its main purpose is the vertex reconstruction, track reconstruction in combination with the TPC and a precise measurement of the charged particle's distance of closest approach (DCA). [19]

- Time Projection Chamber (TPC)

The TPC is divided into A and C side by the central cathode. Two drift chambers, on each side of the cathode, make up a total volume of about 90 m^3 . They are filled

Detector	polar acceptance	azimuthal acceptance	position	main purpose
ITS				
SPD	$ \eta < 2.0$	full	r=3.9 cm	tracking, vertex
	$ \eta < 1.4$	full	r=7.6 cm	tracking, vertex
SDD	$ \eta < 0.9$	full	r=15 cm	tracking, PID
	$ \eta < 0.9$	full	r=23.9 cm	tracking, PID
SSD	$ \eta < 1.0$	full	r=38 cm	tracking, PID
	$ \eta < 1.0$	full	r=43 cm	tracking, PID
TPC	$ \eta < 0.9$	full	$85 < r[cm] < 247$	tracking, PID
TRD	$ \eta < 0.8$	full*	$290 < r[cm] < 368$	tracking, e^{\pm} id
TOF	$ \eta < 0.9$	full	$370 < r[cm] < 399$	PID
PHOS	$ \eta < 0.12$	$220^{\circ} < \phi < 320^{\circ}$	$460 < r[cm] < 478$	photons
EMCal	$ \eta < 0.7$	$80^{\circ} < \phi < 187^{\circ}$	$430 < r[cm] < 455$	photons and jets
HMPID	$ \eta < 0.6$	$1^{\circ} < \phi < 59^{\circ}$	r=490 cm	PID

Table 2: Acceptance, position and purpose of ALICE central-barrel detectors [3] (* In 2012 13 of 18 planned TRD modules were installed, see Figure 7)

with a Ne-CO₂-N₂(85.7 – 9.5 – 4.8%) gas mixture.[7] The TPC covers a radius from 85 cm up to 247 cm around the beam pipe. Because of the central cathode's high voltage of -100 kV, the read out time of the TPC is given by 94 μ s.[9] At the TPC's end plates multi-wire-proportional chambers (MWPC) read out the Inner Readout Chambers (IROC) and Outer Readout Chambers (OROC). Using additional track information from the ITS the TPC is able to fit tracks with a high efficiency even in high multiplicity events. Specific energy loss dE/dx measurements of charged particles are used for PID.

- Transition Radiation Detector (TRD)

Located around the TPC the Transition Radiation Detector's (TRD) is used for electron identification by transition radiation. This ensures a larger statistic for high transverse momentum (p_T) electrons.

Furthermore measurements of specific energy loss dE/dx , charged particle tracking and triggering complete the duties of the TRD. Each of the in 2012 13 installed modules (in 2011 10 modules) consists of six layers of fiber/foam radiator. The TRD is made out of radiator layers, which are read out by multi-wire-proportional chambers MWPC. The MWPCs are filled with a Xe-CO₂ gas mixture. [3]

- Time-Of-Flight detector (TOF)

The outermost detector covering the full azimuthal acceptance is the TOF. Reaching a radius up to 399 cm from the beam pipe it is based on Multigap Resistive Plate Chamber (MRPC) technology.[3]

The time measurements of the TOF detector have a global time resolution of about ~ 80 ps [5] and in conjunction with track and momentum measurements can identify the particle's mass.

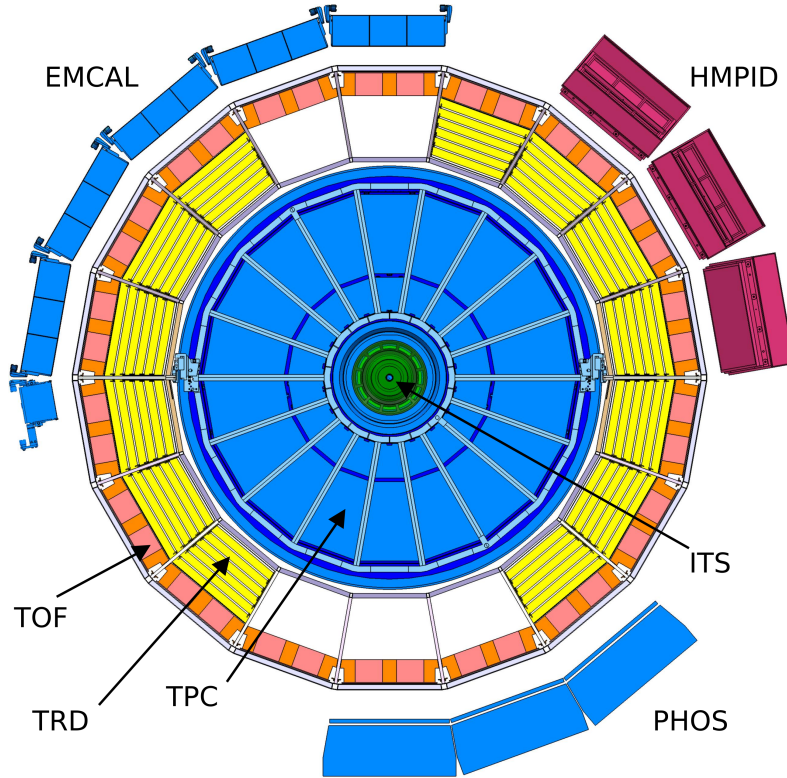


Figure 7: ALICE central-barrel detectors cross section in 2012. In 2011 only 10 of the 13 shown TRD modules have been embedded.[7]

- Photon Spectrometer (PHOS)
PHOS consists of lead tungstate calorimeters, which are read out by avalanche photodiodes. Build at a distance of 4.6 m to the beampipe PHOS main duty is the identification of direct and thermal photons in a momentum range of 100 MeV/c up to 100 GeV/c.[35]
- Electromagnetic Calorimeter (EMCal)
The EMCal covers a pseudorapidity range of $|\eta| < 0.7$ and is made up out of 5 1/3 supermodules in 2012. It is installed at a radius of 4.3 m in respect to the beampipe. Each supermodule consists out of 1152 towers of lead and scintillator layers. The main purpose of EMCal is exploring and measuring jet quenching. Due to its large acceptance for neutral mesons and photons, which is about six times larger than the acceptance of PHOS, it is possible to measure photons and neutral pions up to a transverse momentum of $p_T \sim 30$ GeV/c.[4]

Additionally two VZERO(V0) detectors covering a pseudorapidity range of $-3.7 < \eta < -1.7$ and $2.8 < \eta < 5.1$ are located in z direction at -88 cm and 329 cm in respect to the interaction point. They are made up of plastic scintillators and are mainly used for triggering.[3] The T0 Cherenkov detector measures the longitudinal position and the time of the interaction and the Zero Degree Calorimeter (ZDC) is used to determine centrality in heavy ion collisions.

Detector	Function	Level
SPD	hit-multiplicity based trigger and hit-topology based trigger	L0
TRD	electron trigger, high- p_T particle trigger, charged-jet trigger	L1
TOF	multiplicity trigger, topological (back-to-back) trigger, cosmic-ray trigger	L0
PHOS	photon trigger	L0
EMCal	photon trigger, neutral-jet trigger	L0/L1
ACORDE	cosmic-ray trigger (single and multiple hits)	L0
VZERO	coincidence based minimum-bias interaction trigger, centrality trigger	L0
T0	event-vertex selection trigger, interaction trigger	L0
ZDC	minimum-bias interaction and electromagnetic-dissociation triggers in Pb-Pb	L1
MTR	single-muon trigger, dimuon trigger	L0

Table 3: Trigger characteristics and decision level [3]

3.3 Trigger

Based on detector signals and information about the LHC bunch filling scheme the Central Trigger Processor (CTP) makes its trigger decision. Approximately every 25 ns the CTP analyses the input of the trigger detector. For the level-0 (L0) trigger decision which is done in $\sim 0.9 \mu\text{s}$ the information of VZERO, T0, EMCal, PHOS and the Muon Trigger (MTR) are used. The level-1 (L1) trigger decision is done by the CTP approximately $6.5 \mu\text{s}$ after the L0 decision, which is equal to about 260 LHC clock cycles. Considering the comparatively long L1 decision time, the bottleneck is caused by propagation times of the ZDC which is 113 m away from the interaction point and computation time from TRD and EMCal. Taking the TPC signal into account the level-2 (L2) trigger decision is done approximately $100 \mu\text{s}$ after the collision. Table 3 gives an overview about the different triggers, their main function and their corresponding trigger decision level used by the CTP. In LHC Run 1 every event which was accepted in L1 was also accepted in L2. To suppress background the CTP uses information about the LHC bunch filling scheme. [3]

3.4 Software

Preparing the data and executing the analysis is done using the AliRoot software framework [8]. AliRoot is based on ROOT[29] an object orientated C++ based data analysis program developed at CERN. In order to provide users with the best possible analysis tool ROOT and AliRoot are continuously developed further.

Within the Aliroot software several Monte Carlo (MC) generators, such as Pythia[28] and Phojet[27] are included to simulate single events. For those events the MC generator simulates primary particles with full kinematic information. Then the interactions of those particles traveling through the detector are simulated by GEANT3 [22] and stored with time and location information.

The raw data, which comes from the real detector and from MC simulations is reconstructed in AliRoot for further analysis.[12]

4 Datasets and Photon Reconstruction

In this chapter an overview of the Photon Conversion Method (PCM) is given. Therefore the data and Monte Carlo (MC) datasets which are used for the neutral meson analysis are explained.

4.1 Datasets and Event Selection

The analyzed datasets were taken in 2011-2012 in proton-proton (pp) collisions during Run 1 of the LHC. Each dataset contains periods which correspond to about a month of data taking. The two analyzed datasets include the periods LHC11a and LHC12[a-i].

For the LHC11a dataset the collision energy was $\sqrt{s} = 2.76$ TeV and there are 5.32×10^7 recorded minimum bias events which are used for the analysis. Each minimum bias event was taken with the VZERO OR¹ (MB_{OR}) trigger which requires a hit in one of the two VZERO(V0) detectors or in the SPD.

The second dataset contains the periods LHC12[a-i], which corresponds to 1.15×10^8 recorded minimum bias events at an increased collision energy of $\sqrt{s} = 8$ TeV. For those recorded events the VZERO AND² (MB_{AND}) minimum bias trigger was used. This trigger requires a hit in each of the two VZERO(V0) detectors.

The ALICE offline event selection removes all events which do not originate from physics events (e.g. beam gas interactions or calibration events). In order to reconstruct the primary vertex position of an event it is required that there is at least one contributing track in the Silicon Pixel Detector (SPD) or a global track to the vertex. If the primary vertex position of an event is within ± 10 cm along the beam axis z with respect to the center of the ALICE detector the event is kept, otherwise it is rejected. In order to normalize the spectra the absolute number of events is calculated:

$$N_{norm,evt} = N_{MB,|Z_{Vtx}|<10\text{ cm}} + \frac{N_{MB,|Z_{Vtx}|>10\text{ cm}}}{N_{MB,|Z_{Vtx}|<10\text{ cm}} + N_{MB,|Z_{Vtx}|>10\text{ cm}}} \cdot N_{MB,noVtx} \quad (6)$$

The limiting factor for the data taking rate in ALICE is the TPC's read out time of $\sim 94 \mu\text{s}$ [9], which corresponds to approximately a full turn in the LHC. This leads to overlapping tracks in the central barrel detector, which originate from different events and are referred to as pile up.

Since the start of the LHC's operation time the luminosity of colliding bunches has constantly been increased and therefore the amount of pile up events also increased. Several attempts were made to reduce luminosity for the ALICE experiment. During data taking in 2011 the colliding beams were displaced at the ALICE interaction point. While in 2012 main bunches collided with satellite bunches, that contain a lower number of protons.

Despite the efforts to reduce the luminosity a pile up rejection based on SPD tracks is applied. The SPD pile up rejection removes every event which has more than one reconstructed vertex. This ensures that there are no overlapping events from the same colliding bunches in the central barrel detector. Due to the read out time of the TPC not only

¹V0OR referred to as VZERO OR

²V0AND referred to as VZERO AND

Datasets	\sqrt{s}	MB Trigger	$N_{MB, Z_{Vtx} <10\text{cm}}$	MC event generator
Data				
LHC11 a	2.76 TeV	MB _{OR}	5.32e+07	
LHC12 [a-i]	8 TeV	MB _{AND}	1.15e+08	
MC				
LHC12f1a	2.76 TeV	MB _{OR}	2.77e+07	Pythia
LHC12i3	2.76 TeV	MB _{OR}	1.16e+07	Pythia added signals
LHC12f1b	2.76 TeV	MB _{OR}	2.65e+07	Phojet
LHC14e2a	8 TeV	MB _{AND}	5.25e+07	Pythia
LHC14e2b	8 TeV	MB _{AND}	5.53e+07	Pythia added signals
LHC14e2c	8 TeV	MB _{AND}	5.12e+07	Phojet

Table 4: Datasets

events from the same bunch creating pile up, but also events from other colliding bunches. Therefore an out-of-the bunch pile up correction becomes necessary and will be discussed in chapter 5.2.2.

As part of the quality assurance some runs were not included in the analysis. Deviating dE/dx values in the TPC, a too low number number of photon candidates per event and a wrong π^0 mass were the main reasons to exclude the runs. In the dataset LHC11a 8 of the total 24 runs were excluded which leads to 8.53% loss in statistics. For the 18 of the 492 runs being excluded from the LHC12[a-i] dataset, the loss of statistics is 2.75%. A list of runs used for this analysis can be found in 7.1.

4.1.1 Monte Carlo Simulations

Monte Carlo (MC) simulations are used to correct the data for acceptance and efficiency. For this analysis two different MC event generators Pythia and Phojet are used. Since in the MC single events are simulated, pile up effects do not occur.

- Pythia

Pythia 8.1 is a C++ based MC event generator. It uses perturbative QCD (pQCD) calculations for low and high transverse momentum p_T .

For low p_T the dominant $2 \rightarrow 2$ QCD cross section becomes divergent which is corrected by the existence of a maximum impact parameter and a matter distribution in the hadron interactions at various impact parameters.[20] This version is specialized on LHC physics which does not include γp and $\gamma\gamma$ physics yet and uses the CTEQ5L parton distribution function (PDF).

MC simulations with Pythia describe the evolution of events including initial- and final-state parton showers, multiple parton-parton interactions, string fragmentation, and decays.[32]

The datasets LHC14e2b and LHC12i3 also rely on Pythia MC simulations, but in addition neutral pions π^0 and eta η mesons were added to the Pythia event. Those datasets are referred to as 'added signals'. The signals were added flat in transverse momentum and rapidity. The necessary weighting of the spectrum and the usage of the datasets with added signals is discussed in chapter 5.2.3.

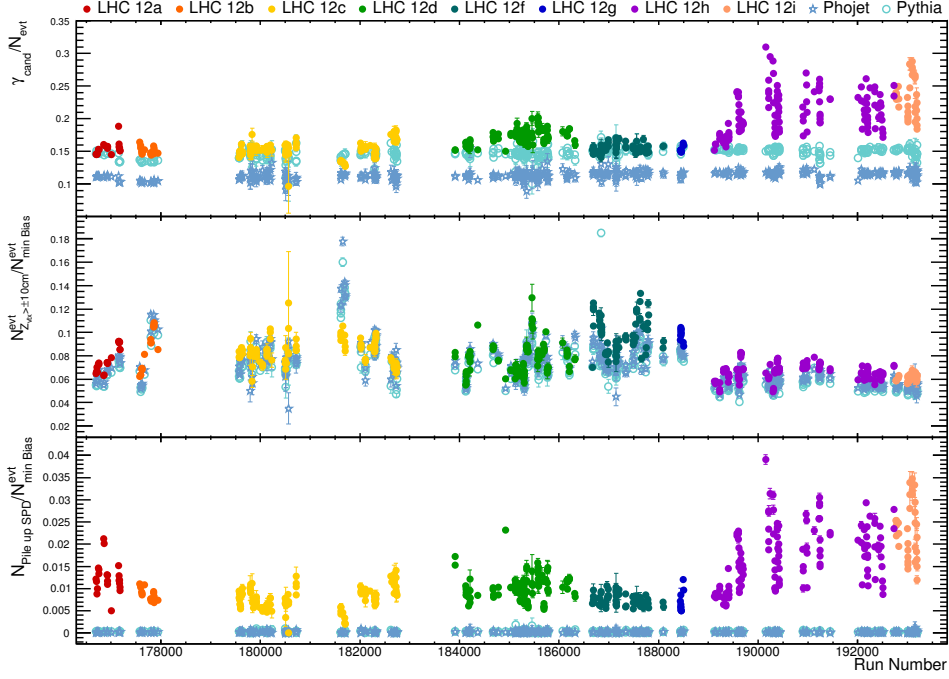


Figure 8: Analyzed runs from LHC12 at $\sqrt{s} = 8 \text{ TeV}$ **Top:** photon candidates per run **Middle:** fraction of events with vertex position outside of 10cm **Bottom:** fraction of rejected events due to SPD pile up rejection

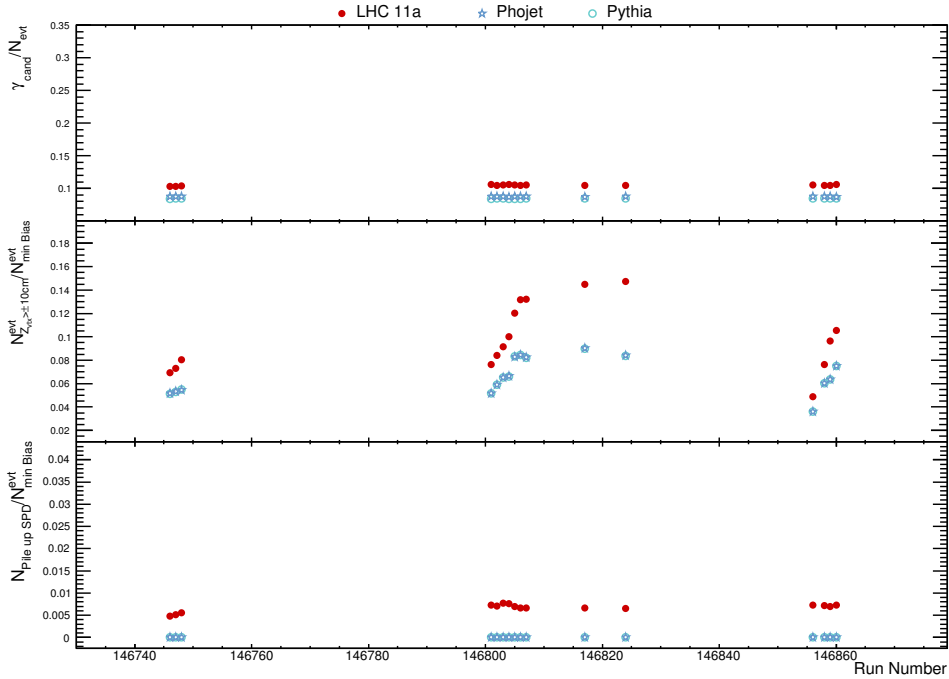


Figure 9: Analyzed runs from LHC11 at $\sqrt{s} = 2.76 \text{ TeV}$ **Top:** photon candidates per run **Middle:** fraction of events with vertex position outside of 10cm **Bottom:** fraction of rejected events due to SPD pile up rejection

- Phojet

The Phojet MC event generator is based on a two component Dual Parton Model (DPM) at low p_T and with a running transition to pQCD at high p_T to avoid the divergence of the dominant $2 \rightarrow 2$ QCD cross section in low transverse momentum p_T . Therefore Phojet is able to describe elastic processes and inelastic processes. The simulation of hadron-hadron, hadron-photon and photon-photon interactions is possible in proton-proton (pp) and antiproton-proton ($\bar{p}p$) events at high energies. [18]

In Figure 8 and Figure 9 the comparison of the MC simulations and the data is shown runwise for the photon candidates, the fraction of vertices with a position outside of ± 10 cm along the beam axis and the number of events rejected due to the SPD pile up rejection. Since the MC event generators simulate single events the fraction of rejected events due to pile up is not reproduced by MC. The deviations of the photon candidates to MC in the periods LHC12h and LHC12i are caused by out of the bunch pile up events.

4.2 Photon Reconstruction

In order to reconstruct the η meson's decay photons first the not identified particles V^0 in the ITS and TPC are selected. Then, based on the track information, the electron e^- and positron e^+ candidates are chosen with which the decay photons are reconstructed. Several cuts at each selection level improve the purity of the photon sample.

4.2.1 Track and V^0 Selection

Track & V^0 cuts	Meson Analysis pp
V0-finder	On-the-Fly
Minimum track p_T	$p_{T,track} > 0.05 \text{ GeV}/c$
$\frac{N_{\text{cluster TPC}}}{N_{\text{findable clusters}}}$	$> 60\%$
η	$ \eta < 0.9$
R_{conv}	$5 \text{ cm} < R_{\text{conv}} < 180 \text{ cm}$
Z_{conv}	$ Z_{\text{conv}} < 240 \text{ cm}$

Table 5: Cuts for track and V^0 selection

The V^0 's are selected with the On-the-Fly V^0 -finder. The advantage over the Offline- V^0 -finder is a better resolution of the conversion point.

For the purpose of selecting just physical reasonable tracks, secondary tracks, which are originating from the V^0 's conversion point, are required to have a no kink topology, comply the TPC refit condition and have opposite charges. In addition the tracks and V^0 candidates have to fulfill the $|\eta| < 0.9$ cut, where η is calculated based on the direction of the photon with respect to the beam axis.

However since the position of the primary vertex is not taken into account some photon candidates which are not in the given fiducial η region will pass through the η cut. Therefore another cut, referred to as line cut, is applied:

$$R_{\text{conv}} > |Z_{\text{conv}}| \times ZR_{\text{slope}} - Z_0 \quad (7)$$

here ZR_{slope} is given by $ZR_{slope} = \tan(2 \times \arctan(\exp(-\eta_{cut})))$. Z_0 is 7 cm and the position of the secondary vertices is calculated to the origin of the ALICE coordinate system (0,0,0).

To improve the track quality, a minimum transverse momentum of 0.05 GeV/ c per track has to be given. Furthermore a minimum fraction of 60% of the findable TPC cluster which are on the track of the electron candidates have to be found. In order to suppress π^0 and η mesons coming from Dalitz decays the conversion radius of the V^0 is required to be larger than 5 cm. The maximum conversion point of $R_{conv} < 180$ cm and $|Z_{conv}| < 240$ cm is chosen to ensure that the conversion can be reconstructed in the TPC. An overview about the analysis cuts applied for the track and V^0 selection is given in Table 5.

4.2.2 Electron Selection

Particle identification PID cuts	Meson Analysis pp
$n\sigma_e$ TPC dE/dx	$-3 < n\sigma_e < 5$
$n\sigma_\pi$ TPC dE/dx	$0.4 \text{ GeV}/c < p < 3.5 \text{ GeV}/c : n\sigma_\pi > 1$ $p > 3.5 \text{ GeV}/c : n\sigma_\pi > -10$

Table 6: Electron Identification cuts

Afterwards the electrons e^- and positrons e^+ have to be identified from the V^0 's. For particle identification (PID) purpose five different main techniques can be used in ALICE:

- dE/dx in the ITS
- dE/dx in the TPC
- time-of-flight measurement with the TOF
- transition radiation or dE/dx measurement in the TRD
- energy deposit in the calorimeters

This analysis is based on dE/dx measurement in the TPC. The other methods were not used due to their limited acceptance in the respective datasets or too low efficiency for low momentum tracks. As the electron sample does not need to be completely pure, the higher statistics justify the electron identification with dE/dx measurements in the TPC. Table 6 shows the PID electron cuts applied on the dE/dx distribution in the TPC. The first PID cut is made around the expected electron energy loss line in orders of σ_e . In this analysis every particle which is $3\sigma_e$ below the expected electron line is rejected. Opening this cut would drastically enlarge the pion contamination. On the other side every particle which is $5\sigma_e$ above the electron line is rejected. With this cut mostly electrons have been chosen.

Additionally a further pion rejection cut is applied. In the momentum (p) interval of $0.4 \text{ GeV}/c < p < 3.5 \text{ GeV}/c$ every particle which is below the $1\sigma_\pi$ mark of the pion line is rejected. This cuts leads to an even higher electron purity.

For high momenta ($p > \sim 4 \text{ GeV}/c$) the pion line slowly merges with the electron line. The

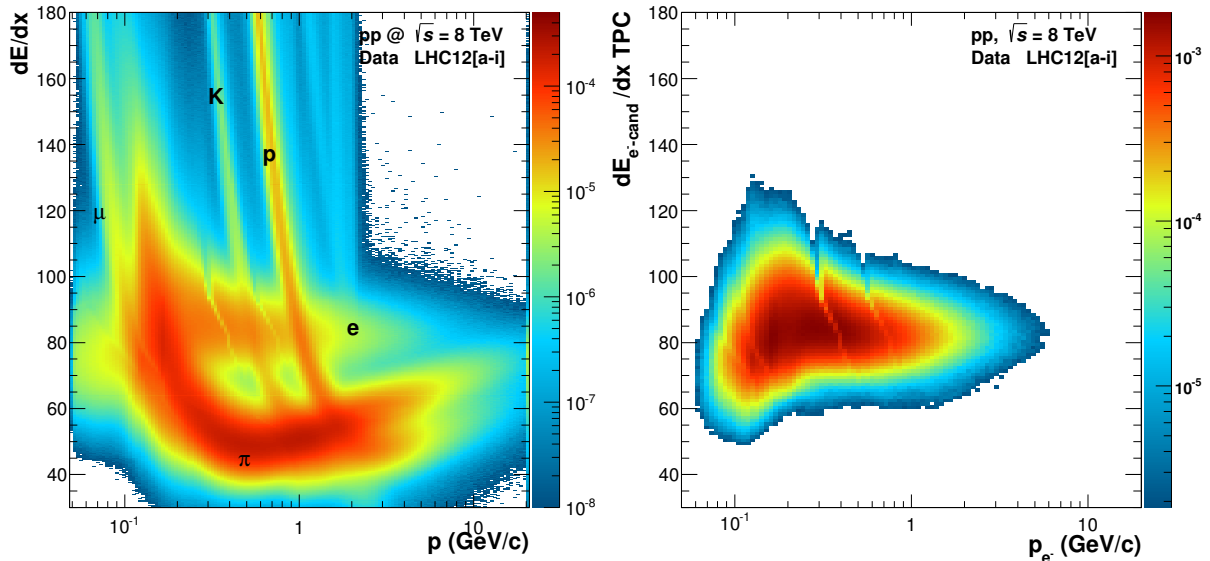


Figure 10: LHC12[a-i]: dE/dx distribution in the TPC before (left) and after (right) the electron PID cuts are applied.

developing problem that the pion rejection cut also removes the electrons in high momenta is solved by opening this cut above $3.5 \text{ GeV}/c$. Above a momentum p of $3.5 \text{ GeV}/c$ every particle which is below the $-10\sigma_\pi$ level of the pion line is rejected. This leads to higher statistics in the high momentum range, but also to a slightly higher pion contaminated electron sample for high momenta electrons. Figure 10 shows the dE/dx distribution of electrons in the TPC at $\sqrt{s} = 8 \text{ TeV}$ before and after the cuts were applied. The plot for $\sqrt{s} = 2.76 \text{ TeV}$ can be found in the Appendix (Figure 29).

4.2.3 Photon Selection

Photon cuts	Meson Analysis pp
2D triangular $\chi_\gamma^2/\text{ndf.}$	< 30
ψ_{pair}	< 0.1
2D elliptical q_T (2D)	$< 0.05 \text{ GeV}/c$
α	< 0.95
$\cos(\text{P.A.})$	> 0.85

Table 7: Photon selection cuts

The photon candidates (V^0 's) are reconstructed in AliRoot by the usage of the KFParticle package. By requiring the χ^2/ndf of the reconstructed photons to be smaller than 30 a cut on the photon quality is done.[13]

The angle between the electrons and positrons momentum plane to the plane perpendicular to the magnetic field is called ψ_{pair} (see Figure 11) and it is defined as [17]:

$$\psi_{\text{pair}} = \arcsin\left(\frac{\Delta\vartheta_0}{\xi_{\text{pair}}}\right) \quad (8)$$

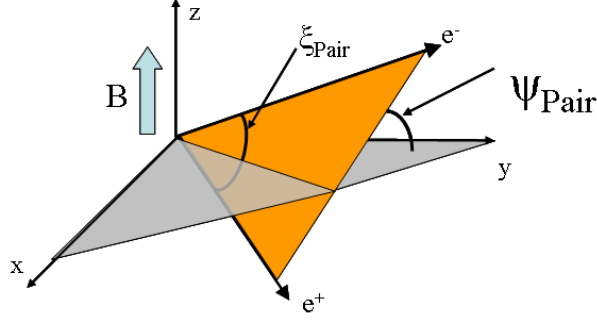


Figure 11: Visualization of the pair ordination in the magnetic field. The x-y plane is orientated perpendicular to the magnetic field.[17]

with,

$$\xi_{\text{pair}} = \arccos \left(\frac{\vec{p}_{e^-} \cdot \vec{p}_{e^+}}{\|\vec{p}_{e^-}\| \cdot \|\vec{p}_{e^+}\|} \right) \quad (9)$$

$\Delta\vartheta_0$ represents the polar opening angle of the electron and positron. Since electrons and positrons originating from pair conversion should not have an opening angle $\Delta\vartheta_0$ and the tracks are bend in opposite directions by the magnetic field, $\Delta\vartheta_0$ is expected to be small and ξ_{pair} to be large. Thus the χ^2/ndf and ψ_{pair} cuts are correlated and in order to gain a clean photon sample a 2 dimensional triangular cut in the χ^2/ndf and ψ_{pair} plane is used. This cut, which is shown in Figure 12, requires χ^2/ndf to be smaller than 30 and ψ_{pair} to be smaller than 0.1.

Furthermore a Cosine Pointing Angle ($\cos(\text{P.A.})$) cut is used in this analysis. To identify its value, first the two secondary track momenta are determined and extrapolated to the V^0 's momentum vector (P). Then it is checked if the momentum vector (P) points to the primary vertex. This is done by building the cosine of the angle between P and the vector R , which points from the primary vertex to the secondary vertex.(see Figure 13) This cut is referred to as Cosine Pointing Angle ($\cos(\text{P.A.})$) cut. In this analysis the $\cos(\text{P.A.})$ is asked to be larger than 0.85.

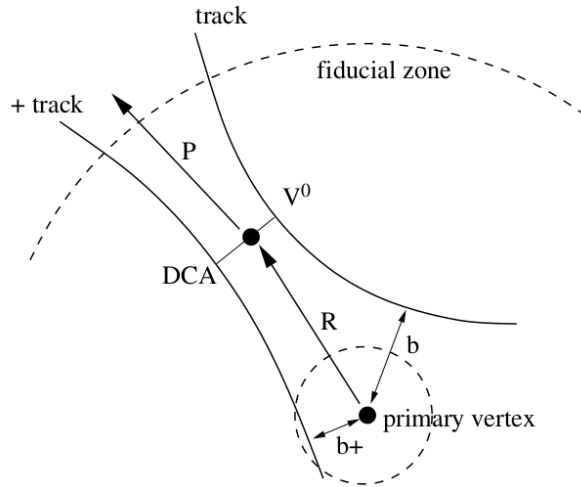


Figure 13: Geometrical selections for track and vertex reconstruction [6]

As the photon sample still includes contaminations of K_S^0 , Λ and $\bar{\Lambda}$ the projection of the momentum of the daughter particle with respect to the mother particle in transverse direction q_T is plotted against the longitudinal momentum asymmetry α . Here q_T and α are given by $q_T = p \times \sin \theta_{mother-daughter}$ and $\alpha = (p_L^+ - p_L^-)/(p_L^+ + p_L^-)$. This plot is called Armentos-Podolanski plot.

Since photons under ideal conditions should have no opening angle q_T should be zero. The distribution for photons should be symmetric in α as the two daughter particles have the same mass. Due to a larger mass of the K_S^0 , Λ and $\bar{\Lambda}$ the momentum projection q_T for those particles should be above zero.

Therefore a two dimensional elliptical cut on $q_T < 0.05 \text{ GeV}/c$ and $\alpha < 0.95$ is applied to select photons. Figure 14 shows the 2 dimensional cut in the Armentos-Podolanski plot for LHC12[a-i]. The Armentos-Podolanski plot for LHC11a can be seen in Figure 30 in the Appendix.

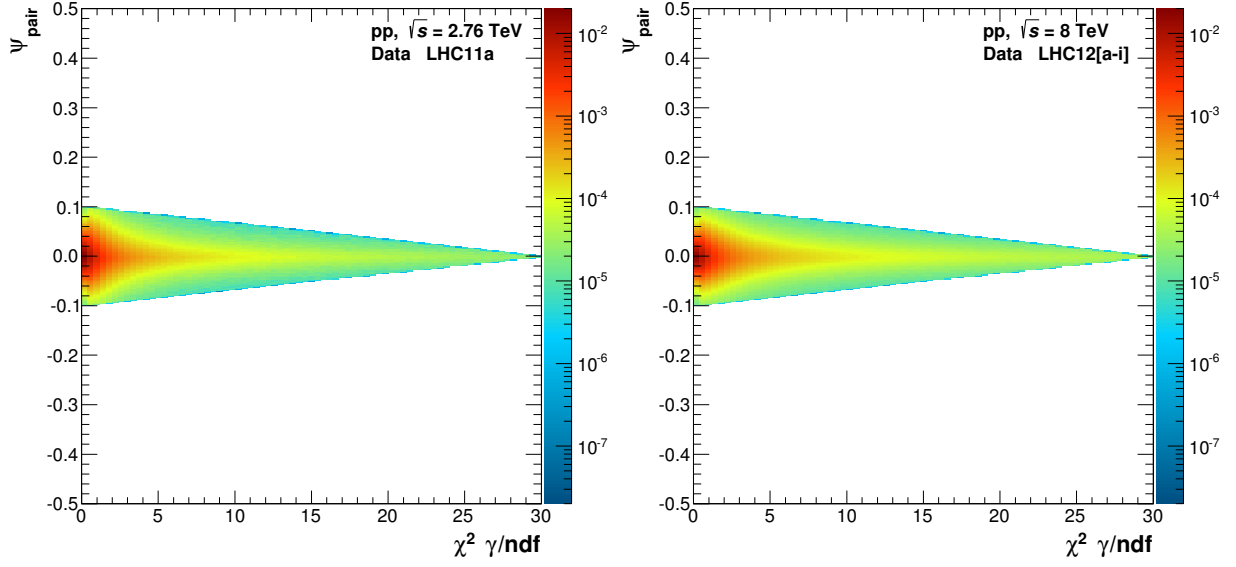


Figure 12: 2D χ^2/ndf and ψ_{pair} cut applied for LHC11a (left) and LHC12[a-i] (right)

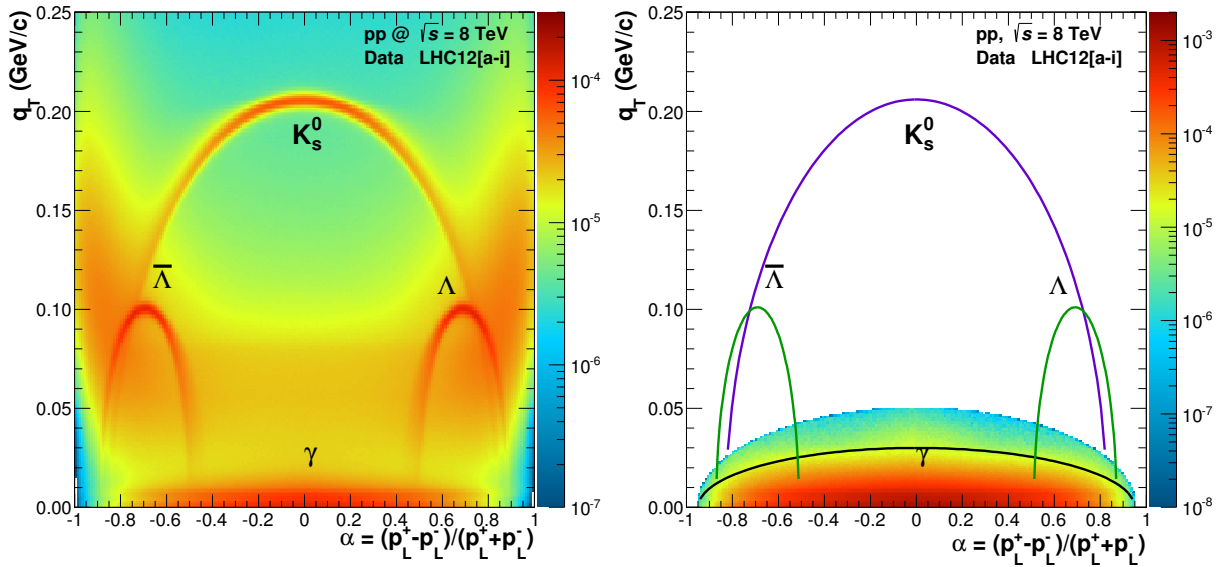


Figure 14: LHC12[a-i]: Armentas-Podolanski-Plot before cuts are applied (left) and after the photon cuts are applied (right)

5 η Meson Analysis

In this chapter the η meson analysis of the 2.76 TeV and 8 TeV datasets is described. In order to extract the η/π^0 ratio, the analysis is also executed for the π^0 meson in the same transverse momentum p_T binning as for the η meson.

The first step is determining the background, which is then subtracted. After that the signal extraction is done. Afterwards the resulting spectrum is corrected for acceptance, efficiency and finite bin width. Furthermore an out-of-the-bunch pile up correction is applied to the data. In addition the π^0 spectrum is corrected for π^0 s originating from secondary vertices.

From the corrected yield the invariant cross section is extracted and compared to NLO calculations. Furthermore the η/π^0 ratio is determined.

5.1 Meson Reconstruction

The in the previous chapter selected photons γ 's are combined into pairs. With the formula

$$M_{\gamma\gamma} = \sqrt{2E_{\gamma_1}E_{\gamma_2}(1 - \cos\theta_{12})} \quad (10)$$

the invariant mass of the photon pairs will be identified using the photons energy $E_{\gamma_{1/2}}$. The angle θ_{12} between the two photons is measured in the laboratory system. Moreover, photon pairs with an opening angle smaller than 5mrad will be excluded from the analysis to remove fake photon candidates. The invariant mass distribution shows a resonance peak coming from the neutral pion π^0 and the η meson at their respective masses of $m_{\pi^0} = 134.9766 \text{ MeV}/c$ and $m_{\eta} = 547.862 \text{ MeV}/c$ [26].

In order to extract the meson's signal the background has to be determined. As the background should be only of combinatorial nature, two methods can be used to calculate it.

- **Event Mixing method**

With the intention to destroy the correlation between the photons, photons from different events are combined to produce the background. It is discovered that the background depends on the event multiplicity and the primary vertex position in Z. Therefore the photons are divided in event multiplicity and Z vertex position bins which are so chosen that every bin contains approximately the same number of photons. Afterwards the photons are combined in their respective Z vertex and multiplicity bins.

- **Rotation method**

The rotation method rotates one photon of a photon pair in azimuthal direction ϕ in the interval $]\pi - \frac{\pi}{9}, \pi + \frac{\pi}{9}[$ by a random number. This rotation will keep the event topology but it will destroy the correlation between the photons.

As the event mixing describes the background better, especially at high transverse momentum p_T , than the rotation method, the event mixing will be used to estimate the background.

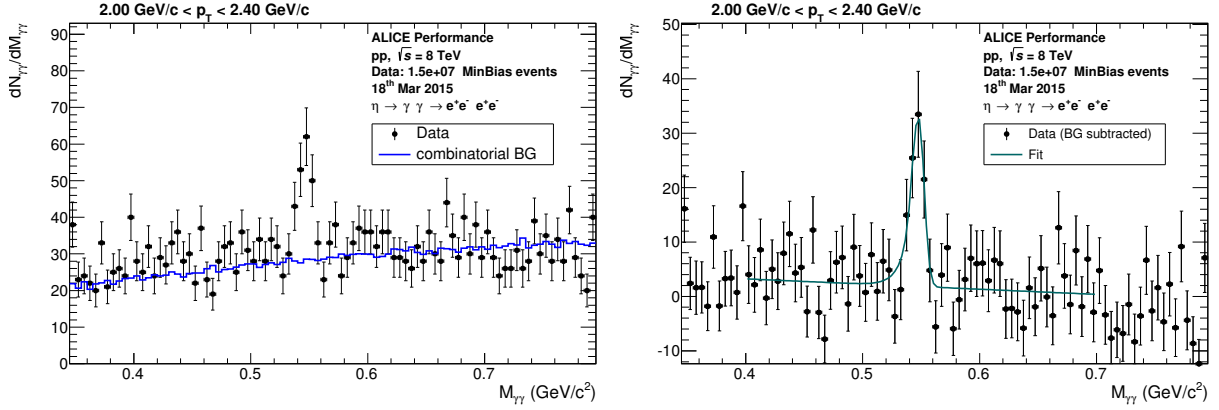


Figure 15: Mixed event background estimation (left) and fit of invariant mass (right) in example bin $2 \text{ GeV}/c < p_T < 2.4 \text{ GeV}/c$ at $\sqrt{s} = 8 \text{ TeV}$

The background created by event mixing has to be normalized close to the meson's peak. It should be done as close as possible to the peak without overlapping with it. Since on the left side of the peak, with a smaller invariant mass, a contribution of bremsstrahlung can be seen, the scaling is done on the right side of the peak. Scaling the background to the left side of the peak also provides a source of systematic uncertainties.

5.1.1 Meson Signal Extraction

The signal extraction is done in transverse momentum bins. The p_T bins reach from $0.5 \text{ GeV}/c$ to $6 \text{ GeV}/c$ for 2.76 TeV and from $0.4 \text{ GeV}/c$ to $8 \text{ GeV}/c$ for 8 TeV .

First the background is determined by event mixing and scaled to the right side of the invariant mass distribution next to the peak. Afterwards the background is subtracted and the remaining distribution is fitted with a modified Gaussian function for each transverse momentum bin. The Gaussian function has an additional exponential term which accounts for the bremsstrahlung tail on the left side of the peak. A linear term describes the remaining background caused by jet correlations.

$$y = A \cdot \left(G(M_{\gamma\gamma}) + \exp\left(\frac{M_{\gamma\gamma} - M_{\pi^0/\eta}}{\lambda}\right) (1 - G(M_{\gamma\gamma}))\theta(M_{\gamma\gamma} - M_{\pi^0/\eta}) \right) + B + C \cdot M_{\gamma\gamma} \quad (11)$$

$$, \text{ with } G = \exp\left(-0.5 \left(\frac{M_{\gamma\gamma} - M_{\pi^0/\eta}}{\sigma_{M_{\gamma\gamma}}}\right)^2\right) \quad (12)$$

A is the amplitude, G a Gaussian function with the standard deviation σ and $M_{\pi^0/\eta}$ stands for the meson's mass. λ adjusts the gradient of the exponential function which is turned off by an Heavyside function $\theta(M_{\gamma\gamma} - M_{\pi^0/\eta})$ above the meson's mass. The remaining term $B + C \cdot M_{\gamma\gamma}$ is the linear function including the remaining background.

From the fit parameters the invariant mass and the full width at half maximum, which

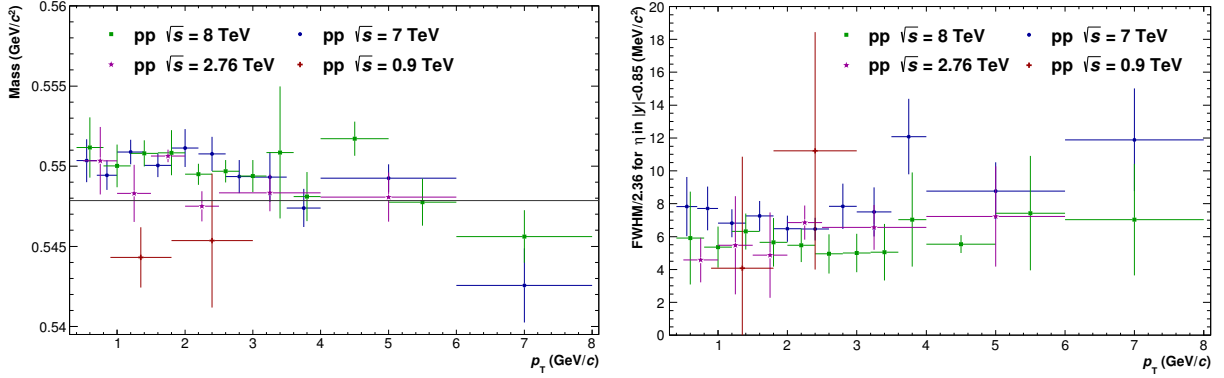


Figure 16: Invariant mass (left) and full width half maximum (right) distribution for the η meson 900 GeV, 2.76 TeV, 7 TeV and 8 TeV. The data for 900 GeV and 7 TeV is taken from [2]

corresponds to the resolution of the peak, can be extracted for each p_T bin. The invariant mass for each bin in p_T can be seen in Figure 16. In order to extract the meson's yield, the remaining linear background is subtracted and an integration around the peak is done. For the neutral pion the integration is fulfilled in the interval $(M_{\pi^0} - 0.035 \text{ GeV}/c, M_{\pi^0} + 0.010 \text{ GeV}/c)$ and for the η meson with a larger width and therefore a larger interval of $(M_{\eta} - 0.048 \text{ GeV}/c, M_{\eta} + 0.022 \text{ GeV}/c)$. Through the asymmetric integration window the tail caused by bremsstrahlung accounts to the integral. To obtain the raw yields an integration over the the different integration windows is performed:

$$N_{\text{raw}}^{\pi^0/\eta} = \int (N^{\gamma\gamma} - N^{\text{comb. BG}}) dM_{\gamma\gamma} - \int (B + C \cdot M_{\gamma\gamma}) dM_{\gamma\gamma} \quad (13)$$

The measured raw yield spectra for the η meson can be seen in Figure 17.

5.2 Spectra Corrections

As the measured raw yield spectra is influenced by some effects which should not account to the η meson's yield, it needs to be corrected for them. At first the π^0 raw yield spectrum is corrected for the fraction of secondary pions, which do not originate from the primary vertex. Then an out-of-the bunch pile up correction is applied for the η and π^0 meson. Afterwards the effects of the geometrical acceptance and the efficiency to the spectra are determined and corrected. Finally a correction for the finite bin width of the transverse momentum is discussed.

5.2.1 Secondary Pions Correction

Neutral pions do not always come from the primary collision vertex. Instead they also can originate from weak or hadronic interactions from particles of the first generation. Therefore the π^0 raw yield has to be corrected for pions coming from secondary vertices. With an branching ratio of 30.7% the decay $K_s^0 \rightarrow \pi^0\pi^0$ depicts the largest contribution of neutral pions from secondary vertices. The contribution is determined and corrected

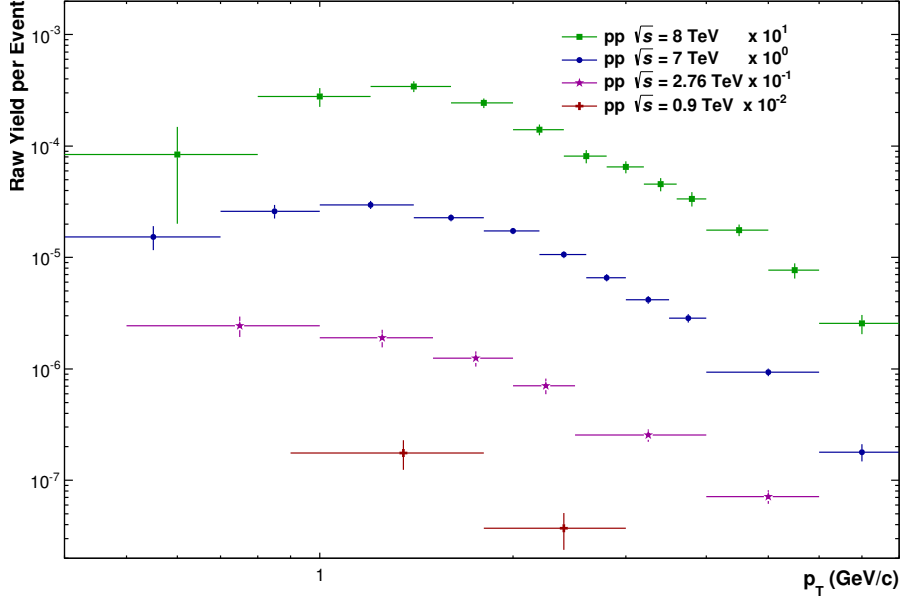


Figure 17: η meson raw yield spectra normalized to $N_{\text{evt.}}$ for 900 GeV, 2.76 TeV, 7 TeV and 8 TeV. The raw yield spectra for 900 GeV and 7 TeV are taken from [2]

using the MC simulations. Figure 18 shows the amount of secondary neutral pions from K_s^0 in dependence on the transverse momentum p_T . Since the MC simulations do not describe the K_s^0 spectra correctly and underestimate it, this mismatch should be corrected in the future.

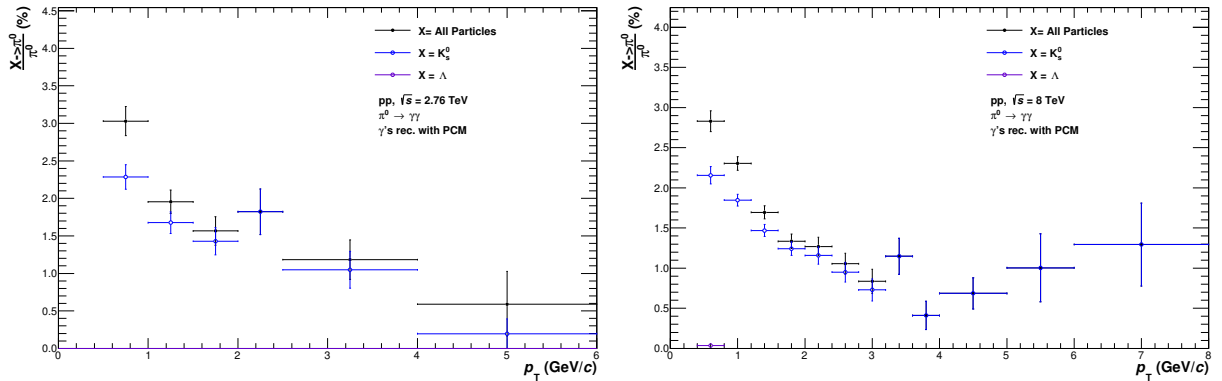


Figure 18: Fraction of secondary π^0 mesons from K_s^0 (blue) or all secondary π^0 (black) to the total number of reconstructed π^0 for 2.76 TeV (left) and 8 TeV (right)

5.2.2 Out of the Bunch Pile Up Correction

With increasing luminosity and a more and more compact filling scheme, the LHC provides a continuously increasing event rate in the ALICE detector. Due to the charges drift velocity of $2.7 \text{ cm}/\mu\text{s}$ in the TPC, the TPC has a read out time of approximately $94 \mu\text{s}$ [9]. Since the read out time corresponds to a full turn in the LHC, the issue of overlapping

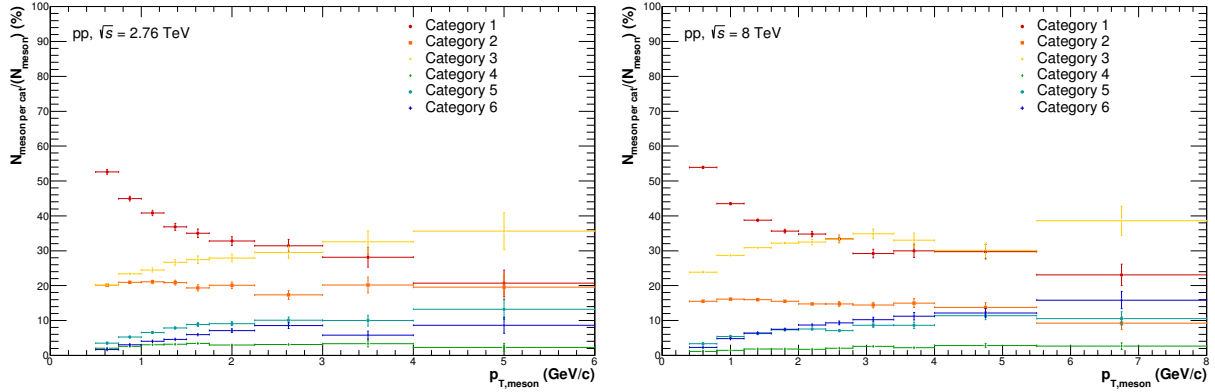


Figure 19: Distribution of meson categories in dependence of p_T for LHC11a(left) and LHC12[a-i](right)

tracks in the TPC, that create a huge amount of pile up, becomes important.

The pile up created in the same bunch can be rejected by the usage of the SPD pile up rejection with its short integration time of 200 ns (see chapter 4.1). Because of the TPC's read out time pile up is not only created in the same bunch. Therefore a correction for the out of the bunch pile up becomes necessary.

For determining the amount of pile up the distance of closest approach (DCA) in z -direction (dca_z) is used (see Figure 13). Events which do not come from the triggered minimum bias event are due to the TPC's charge drift time seen as shifted in z and are therefore visible as a background in the dca_z distribution. Since the pile up events are seen as shifted in z most of them will not pass the cosine pointing angle cut $\cos P.A$, which reduces the amount of expected pile up.

In order to correct for the pile up, the amount of background in the dca_z distribution has to be identified for each transverse momentum p_T bin.

This can be seen for the η meson in Figure 35 and 36 in the Appendix for 2.76 TeV and 8 TeV. The pions dca_z background estimation can be found in Figure 37 and 38.

As the reconstructed photons in ALICE can be grouped in three different categories, they all give their own contribution to the dca_z distribution:

1. The photon converts in the TPC and the electron tracks are just found in the TPC.
2. At least one electron has two hits in the ITS
3. Both electrons have hits in the ITS

In principle the contribution of category 2 should be smaller than category 3 since it is very unlikely to have one electron track in the ITS, while the other one does not appear in the ITS. But due to the possibility of two electrons passing through the same ITS cluster and therefore get detected as one electron and dead areas in the ITS, category 2 makes up a similar amount of photons as category 3.

Since there are three categories of photons, the reconstructed mesons can be divided in six different categories:

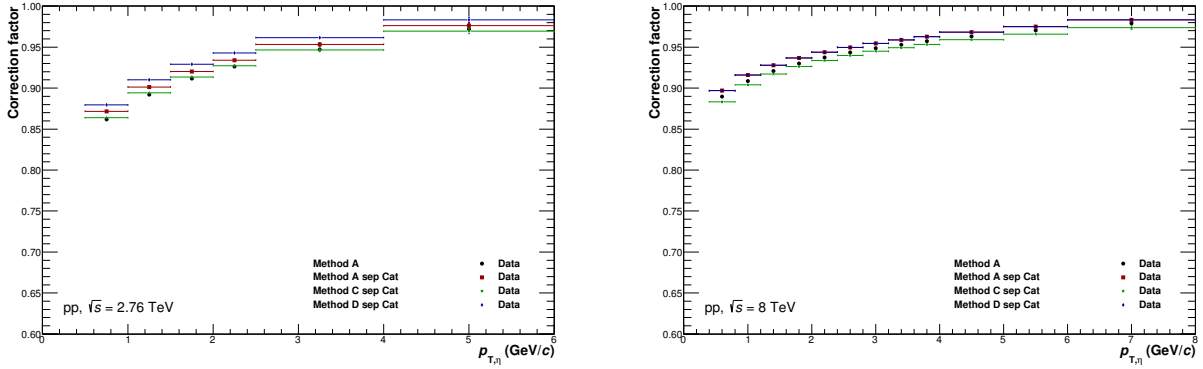


Figure 20: p_T dependent pile up correction factor for LHC11a(left) and LHC12[a-i](right)

1. Both photons come from category 1
2. One photon of category 1 and one of category 2
3. One photon of category 1 and one of category 3
4. Both photons come from category 2
5. One photon of category 2 and one of category 3
6. Both photons come from category 3

The distribution of the different categories, dependent on the transverse momentum p_T , can be seen in Figure 19. Due to the fact that all categories, except for category 1, require ITS information, their contribution to the amount of pile up is suppressed. Category 6 should have no pile up since both photons have ITS information. But however it makes up a small amount to the total fraction of reconstructed mesons. The categories contribution to the pile up can be seen in Figure 39 in the Appendix.

To estimate the background from the dca_z bins three different methods can be used:

- **Method A**

This method uses the member function 'ShowBackground' implemented in the TH1 class of root. It determines the background under a given peak. The smoothing option for this member function and analysis is set to 'BackSmoothing9'.

- **Method B**

A Gaussian with a hole around the peak region of 0 is fitted to the dca_z distribution. In order to ensure a good fit and determine the correct amount of background a large statistic is needed for this method.

- **Method D**

Uses the same member function 'ShowBackground' as method A but with a higher smoothing. ('BackSmoothing11')

The total correction factor for the different methods can be seen in Figure 20. With a higher transverse momentum p_T the contribution of pile up is decreasing. This is because at low p_T the contribution of category 1 mesons, which contributes the highest amount of pile up, is the largest. In this analysis Method A is used to determine the background.

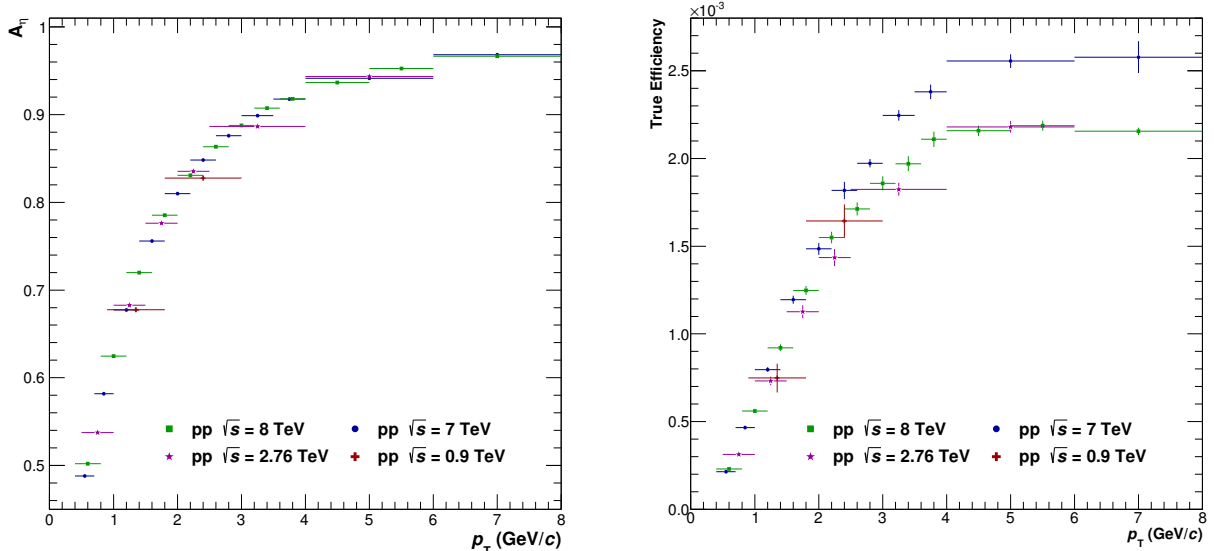


Figure 21: η meson acceptance (left) and efficiency (right) for 900 GeV, 2.76 TeV, 7 TeV and 8 TeV. The acceptance and efficiency for 900 GeV and 7 TeV is taken from [2]

5.2.3 Corrections for Acceptance and Efficiency

As the detector has limited geometrical acceptance and reconstruction efficiency, corrections on the raw yield have to be done. The acceptance $A_{\pi^0/\eta}$ is given by the ratio of π^0/η mesons within the rapidity window $|y| < 0.8$ with daughter particles found in the pseudorapidity window of $|\eta| < 0.9$ to all π^0/η mesons originating in this rapidity range.

$$A_{\pi^0/\eta} = \frac{N_{\pi^0/\eta, |y| < y_{\max}} \text{ with daughter particles within } |\eta_\gamma| < 0.9}{N_{\pi^0/\eta, |y| < y_{\max}}} \quad (14)$$

The acceptance is calculated using the MC simulations and can be seen in Figure 21 for 900 GeV, 2.76 TeV, 7 TeV and 8 TeV. As the acceptance of the TPC and ITS did not change during data taking of the different datasets at different energies, no significant deviation in the acceptance can be seen.

The reconstruction efficiency is defined as

$$\epsilon_{reco, \pi^0/\eta} = \frac{\text{verified } N_{\pi^0/\eta, rec}(p_T, rec)}{N_{\pi^0/\eta, |y| < y_{\max}} \text{ with daughter particles within } |\eta_\gamma| < 0.9(p_T, MC)} \quad (15)$$

To determine the true number of π^0/η mesons, produced with photons in the pseudorapidity window of $|\eta| < 0.9$, Monte Carlo (MC) simulations are used. Here the datasets of the generators Phojet and Pythia are both taken into account. As the number of events at high p_T decreases the statistical error on the efficiency would increase a lot. Therefore a MC simulation with added π^0 and η mesons (periods LHC12i3 and LHC14e2b) is used to gain statistics at high p_T .

The added signals are added flat in p_T and y , which makes it necessary to reweigh them according to the true spectral shape. First the data spectrum is fitted. Then the ratio of the MC and MC with added signals to the fit is build which is used as input for the weighting procedure done in AliRoot. Several iterations are needed to reweight the MC spectra correctly.

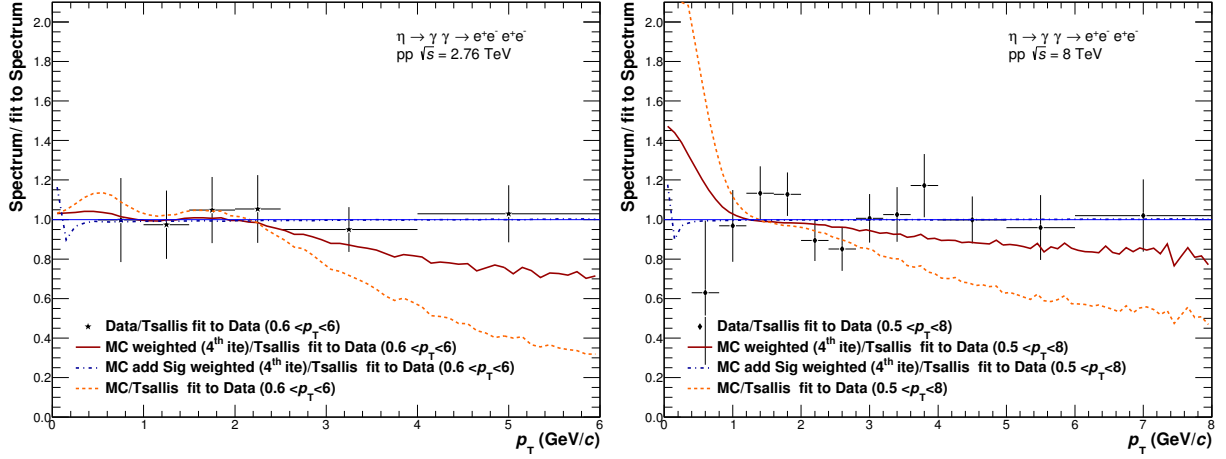


Figure 22: Ratio of weighted η meson MC spectra with and without added signals to fit after the 4th iteration. LHC11a (left) and LHC12[a-i] (right)

In Figure 22 the ratio of the weighted MC with and without added signals to the fit after the last (4th) iteration is shown for the η meson. Figure 40 in the Appendix shows them for the π^0 . After the 4th iteration the spectra of the added signals does not deviate from the fit to the data and describes a flat line. Above ~ 3 GeV/ c the reweighted MC spectra for the η meson shows a decreasing trend.

The efficiency is calculated in each transverse momentum p_T bin for the minimum bias MC dataset and for the MC added signals separately. Then the final efficiency is build by merging the minimum bias efficiency and added signals efficiency according to their statistical error.

Since the error of the minimum bias spectra is large for high p_T (above 3 GeV/ c) its contribution becomes marginal. As there is only minor influence of the minimum bias efficiency at high p_T , the reweighted spectra can be used for efficiency calculations. A comparison of the weighted to the unweighted spectra can be found in Figure 23. The final merged efficiency for the η meson is shown in Figure 21.

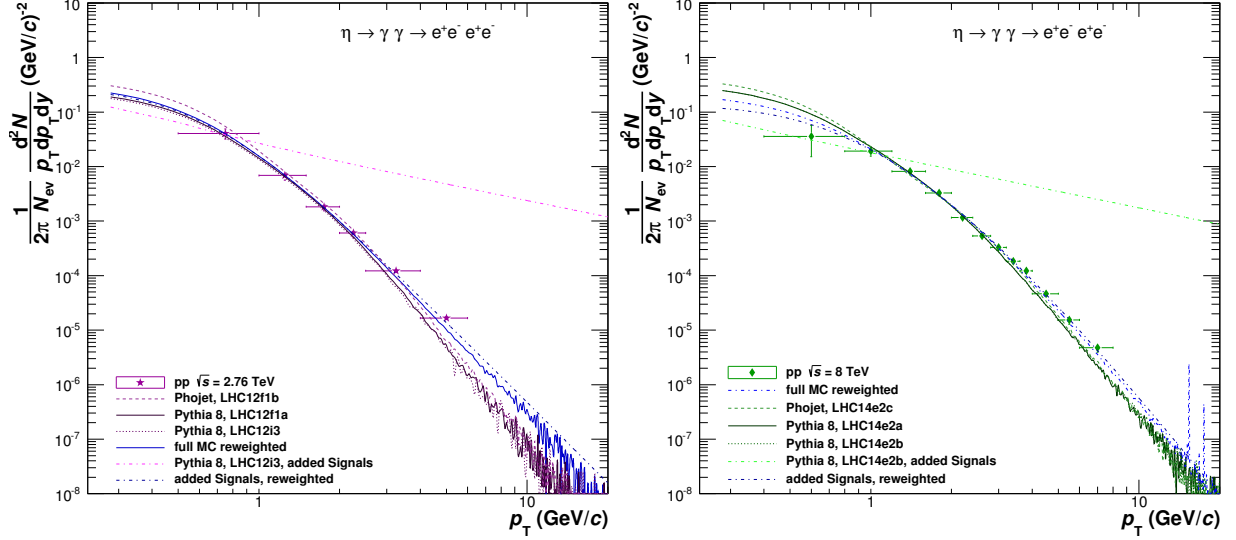


Figure 23: Comparison of minimum bias, weighted MC with and without added signals and unweighted MC added signals spectra for the η meson for LHC11a (left) and LHC12[a-i] (right). The comparison of the spectra for the π^0 meson can be found in the Appendix in Figure 41

5.2.4 Correction for finite bin width

The η meson spectra decreases not linear with larger transverse momentum p_T . As the spectra is binned in p_T the value of the middle of a bin will not correspond to its true value. To correct for this a bin shift along the transverse momentum is applied so that the value at the middle of the bin represents the true value. For an approximation of the true yield spectrum a Tsallis[33] function is used:

$$\frac{d^2N}{dydp_T} = \frac{(n_{Tsallis} - 1)(n_{Tsallis} - 2)}{n_{Tsallis}T[n_{Tsallis}T + m(n_{Tsallis} - 2)]} \times A \times p_T \times \left(1 + \frac{m_T - m}{n_{Tsallis}T}\right)^{-n_{Tsallis}} \quad (16)$$

With m and $m_T = \sqrt{m^2 + p_T^2}$ as particle and transverse mass, and A, T and $n_{Tsallis}$ as free fit parameters. The size of this correction depends on the bin width and the slope of the spectra.

5.2.5 Systematic Error Evaluation

To extract the systematic error, each cut for the track, electron, photon and meson selection has been varied in order to obtain the maximum possible deviation or in the case of Gaussian distributions to reflect the standard deviation. Since only one cut is changed at a time the effect on the systematic error for each cut variation will be extracted and estimated for each bin in transverse momentum.

$$\Delta(p_T) = \left(\frac{d^2N}{dydp_T}\right)_{modified}(p_T) - \left(\frac{d^2N}{dydp_T}\right)_{standard}(p_T) \quad (17)$$

$$\sigma_{\Delta}(p_T) = \sqrt{\left| \sigma^2\left(\frac{d^2N}{dydp_T}\right)_{modified}(p_T) - \sigma^2\left(\frac{d^2N}{dydp_T}\right)_{standard}(p_T) \right|} \quad (18)$$

For each cut variation the systematic error is calculated bin by bin. Therefore the maximum deviation compared to the standard cut in positive and negative direction was determined. Then the average value from the absolute maximum deviation in positive and negative direction is build. Table 8 shows all cut variations which were used to evaluate the systematic error. There are five major contributions to the systematic error:

Material Budget

In previous Analysis at 2.76 TeV the systematic error for the material budget has been estimated to 9.00% in proton-proton (pp) collisions over the whole transverse momentum range.[12] Due to the fact that the error of the material budget changes with R, there will be no separate cut variation on the R cut.

Signal Extraction

The signal extraction includes the mesons energy asymmetry α cut and the two different methods to estimate the background. Since the normalization of the background is done at the right side (standard) of the peak it is changed to the left side as an additional systematic error source. Furthermore the integration window for determining the yield is modified in a narrow and wide integration window. The yield extraction is one of the larger error sources and contributes over 10% for some transverse momentum bins.

Integration window	η	π^0
Narrow	$(M_{\eta} - 0.033, M_{\eta} + 0.012)\text{GeV}/c^2$	$(M_{\pi^0} - 0.015, M_{\pi^0} + 0.005)\text{GeV}/c^2$
Normal	$(M_{\eta} - 0.048, M_{\eta} + 0.022)\text{GeV}/c^2$	$(M_{\pi^0} - 0.035, M_{\pi^0} + 0.010)\text{GeV}/c^2$
Wide	$(M_{\eta} - 0.068, M_{\eta} + 0.032)\text{GeV}/c^2$	$(M_{\pi^0} - 0.055, M_{\pi^0} + 0.025)\text{GeV}/c^2$

Track Reconstruction

In this category the systematic errors coming from the minimum p_T and findable TPC cluster cuts are summarized. It contributes up to $\sim 5\%$ at low p_T for the LHC11a data. At high p_T and in the LHC12[a-i] dataset, this category contributes about $\sim 3\%$ to the systematic error.

Electron Selection

The electron selection summarizes the electron PID cuts as the electron dE/dx cut and the pion rejection cut in the TPC

Photon Reconstruction.

The cut variations for the $q_{T,max}, \chi^2 \gamma$ and ψ_{pair} cut contribute to this category. Since the 2 dimensional triangular $\chi^2 \gamma$ and ψ_{pair} cut are correlated they are varied together. Its share to the systematic error add up to $\sim 10\%$ at low p_T and decreases at mid and high p_T to $\sim 3\%$.

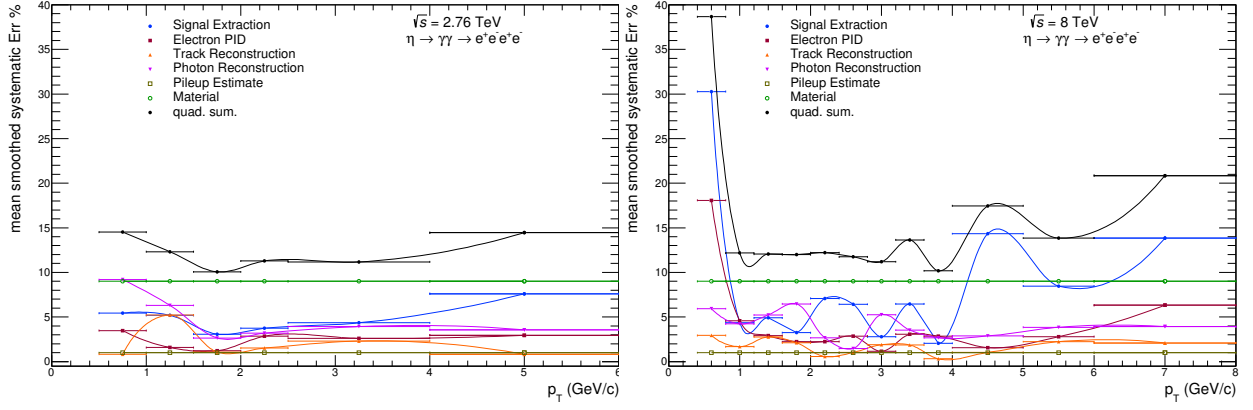


Figure 24: η meson systematic error for each bin in p_T for LHC11a (left) and LHC12[a-i] (right)

The systematic errors for the η meson in each bin in p_T can be found in Figure 24. A detailed visualization of the single cut variations share to the systematic error for the π^0 and η meson can be found in the Appendix 7.7. For 2.76 TeV the quadratically summed error is in the range of ~ 10 -15% while for 8 TeV the error is similar except for low and high p_T . The largest contribution to the first bin is the signal extraction with $\sim 30\%$ and the electron PID with $\sim 18\%$. This leads to an overall systematic error of nearly 40% for the first bin, which shows the challenge of signal extraction at low p_T .

Quantity	Standard	Cut 1	Cut 2	Cut 3
single p_T e^\pm	> 0.05 GeV/c	> 0.075 GeV/c	> 0.1 GeV/c	
min. TPC cluster/ find. TPC cluster	$> 60\%$	$> 35\%$	$> 70\%$	
dE/dx TPC e-line				
$n\sigma_{dE/dx,e}$	$-3 < n\sigma_e < 5$	$-4 < n\sigma_e < 5$	$-2.5 < n\sigma_e < 4$	
dE/dx TPC π-line				
$p_{\min,\pi}$ rej.	0.4 GeV/c	0.5 GeV/c		
$p_{\max,\pi}$ rej.	3.5 GeV/c	5 GeV/c		
$n\sigma_{dE/dx,\pi}$ rejection	$n\sigma_\pi > 1$	$n\sigma_\pi > 2$	$n\sigma_\pi > 0$	
high p $\sigma_{dE/dx,\pi}$ rej.	$n\sigma_\pi > -10$			
$q_{T,\max}$	< 0.05 GeV/c (2D)	< 0.07 GeV/c (1D)	< 0.03 GeV/c (2D)	< 0.05 GeV/c (1D)
χ^2_γ	< 30	< 50	< 20	< 30
ψ_{pair}	< 0.1 (2D)	< 0.2 (2D)	< 0.05 (2D)	< 0.1 (1D)
α meson	< 1	< 0.85		

Table 8: Cut variations compared to the standard cut. In order to evaluate the systematic errors only one cut is changed at a time. (Except for χ^2_γ and ψ_{pair} cut as they are highly correlated)

5.3 Corrected Spectra and Comparison to Theory

After applying all mentioned corrections the corrected yield for $\eta \rightarrow \gamma\gamma$ is calculated with the formula

$$\frac{1}{2\pi} \frac{1}{p_T} \frac{d^2 N}{dy dp_T} = \frac{1}{2\pi} \frac{1}{N_{evt.}} \frac{1}{p_T} \frac{1}{\epsilon_{\pi^0/\eta}} \frac{1}{A_{\pi^0/\eta}} \frac{1}{BR} \frac{1}{\Delta y \Delta p_T} N^{\pi^0/\eta} \quad (19)$$

Here $N_{evt.}$ stands for the number of events, $\epsilon_{\pi^0/\eta}$ for the mesons efficiency and $A_{\pi^0/\eta}$ for the mesons acceptance. The branching ratio of the $\eta \rightarrow \gamma\gamma$ process is respected by BR while $N^{\pi^0/\eta}$ describes the number of reconstructed mesons in the interval $\Delta y \Delta p_T$. The corrected yield for the η meson can be seen in Figure 25.

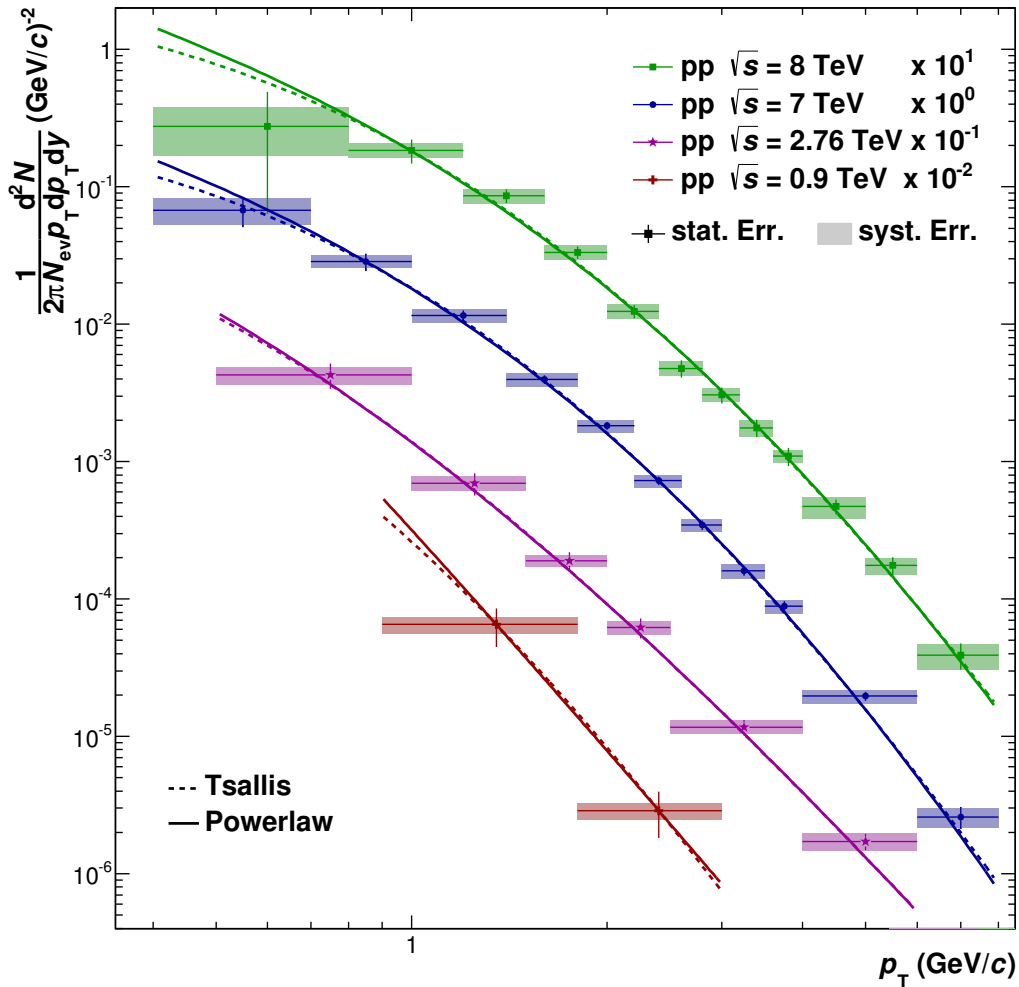


Figure 25: Full corrected differential invariant η meson yield for 900 GeV, 2.76 TeV, 7 TeV and 8 TeV normalised to the number of events. The spectra for 900 GeV and 7 TeV are taken from [2]

The error bars represent the statistical errors while the boxes account for the systematic errors. The spectra has been fitted to a Tsallis (dotted line, Equation 16) and Powerlaw

(continuous line) function. The Powerlaw fitting function is given

$$E \frac{d^3 N}{dp^3} = A_{pow} \cdot \frac{2(n_{pow} - 1)(n_{pow} - 2)(n_{pow} - 3)^2}{\pi p_T} \left(\frac{1 + 2p_T}{\langle p_T \rangle (n_{pow} - 3)} \right)^{-n_{pow}} \quad (20)$$

with A_{pow} , n_{pow} and $\langle p_T \rangle$ as free fitting parameters. In order to compare the corrected η meson yield at 0.9 TeV (preliminary) and 7 TeV, published in [2], with the extracted yields from this analysis at 2.76 TeV and 8 TeV, they are both shown in the same plot. Moreover, the differential invariant cross section can be extracted with the formula:

$$E \frac{d^3 \sigma}{dp^3} = \frac{1}{2\pi} \frac{\sigma_{AND/OR}}{N_{evt.}} \frac{1}{p_T} \frac{1}{\epsilon_{rec,\eta}} \frac{1}{A_\eta} \frac{1}{BR} \frac{N^\eta}{\Delta y \Delta p_T} \quad (21)$$

Here the number of events for normalization are referred to as $N_{evt.}$, BR stands for the branching ratio of the η meson decay to two photons $\eta \rightarrow \gamma\gamma$ and $\sigma_{AND/OR}$ for the cross section of the used minimum bias trigger.

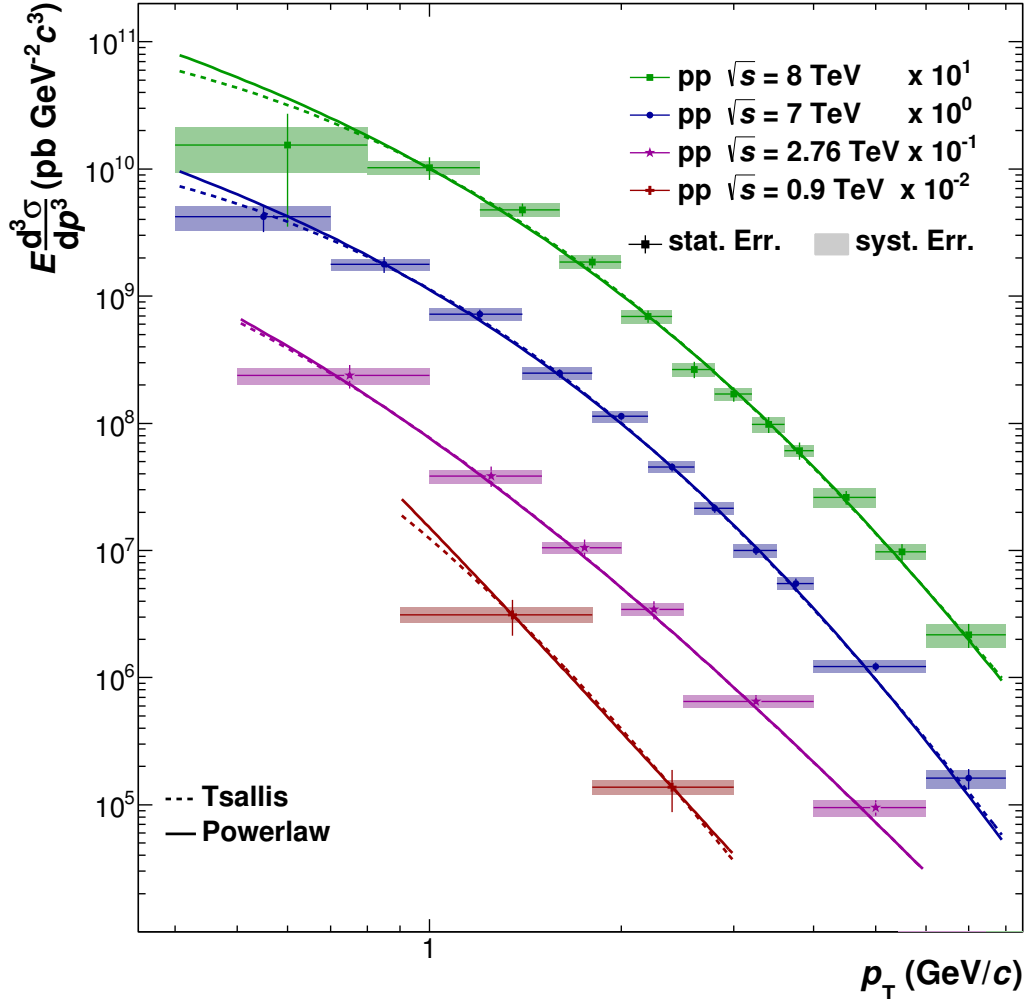


Figure 26: η meson invariant cross section for 900 GeV, 2.76 TeV, 7 TeV and 8 TeV. The spectra for 900 GeV and 7 TeV is taken from [2]

Both fitting functions represent the corrected invariant yield well, except for the first transverse momentum bin $0.4 \text{ GeV} < p_T < 0.8 \text{ GeV}$ at 8 TeV. Although the statistical and systematic errors for that bin are large, it illustrates the difficulties of the signal extraction at the low transverse momentum region.

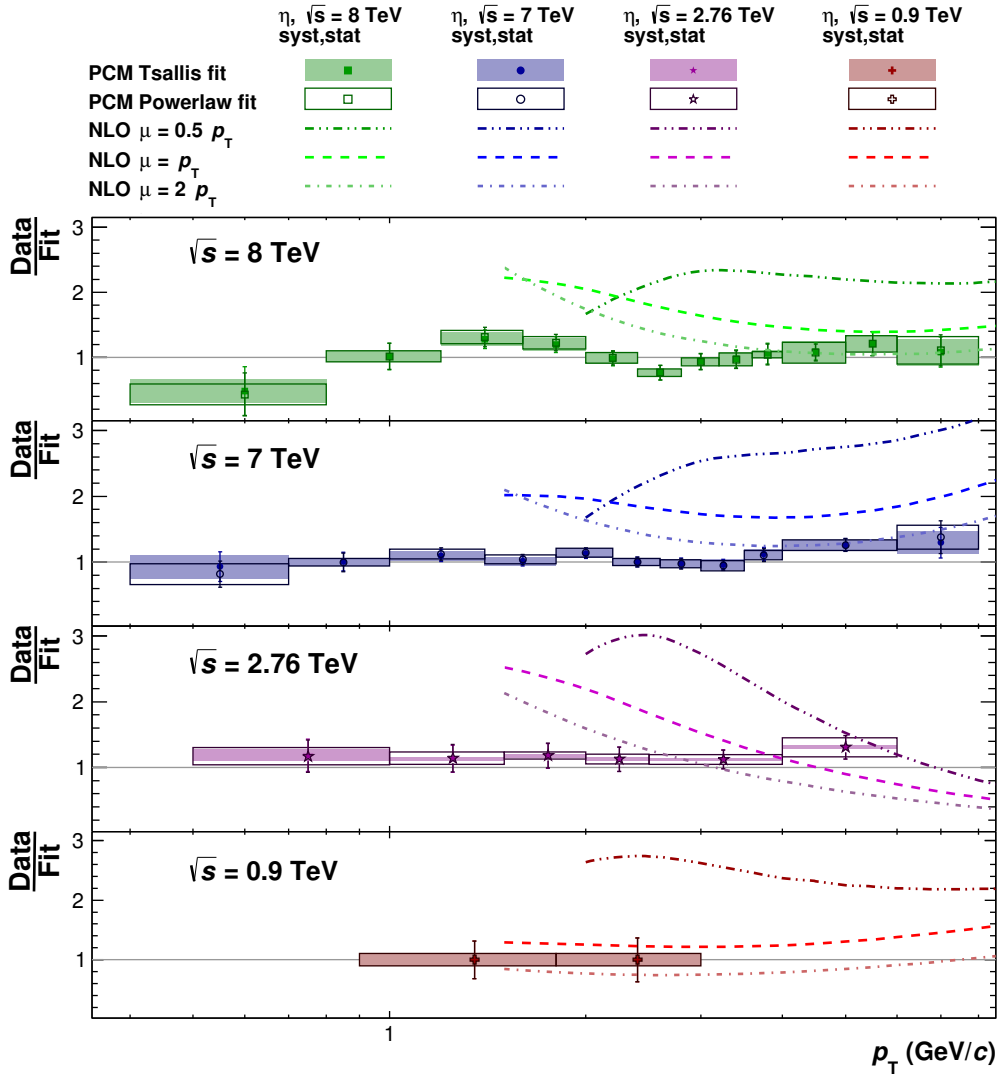


Figure 27: η meson ratio of data to Tsallis/Powerlaw fit. Dotted lines are NLO calculations to Tsallis fit. The spectra for 900 GeV and 7 TeV are taken from [2]

For LHC11a σ_{OR} has been determined to $(55.416) \mu\text{b}$ and for LHC12[a-i] σ_{AND} to $(55.74 \pm 0.46) \mu\text{b}$ [10]. The term $N^\eta/\Delta y \Delta p_T$ accounts for the raw yield measured in a rapidity range of $[-0.8, 0.8]$ and the transverse momentum bin Δp_T .

The extracted invariant cross section for the energies 900 GeV, 2.76 TeV, 7 TeV and 8 TeV can be seen in Figure 26. Figure 27 shows the data points divided by the Tsallis and Powerlaw fit, respectively.

Furthermore the NLO calculations with different parameters for μ are shown. The maximum deviation by a factor of ~ 2 -3 for the analyzed datasets can also be seen in the previous measurements at 0.9 TeV and 7 TeV.

5.4 η/π^0 Ratio

Building the η/π^0 ratio provides us with information about the production of particles. As the π^0 spectra is corrected the same way as the η spectra in the respective binning, the η/π^0 ratio can be seen in Figure 28 for 900 GeV, 2.76 TeV, 7 TeV and 8 TeV.

Above $\sim 4 \text{ GeV}/c$ a positive deviation for the 2.76 TeV and 8 TeV datasets compared to the 7 TeV dataset can be seen.

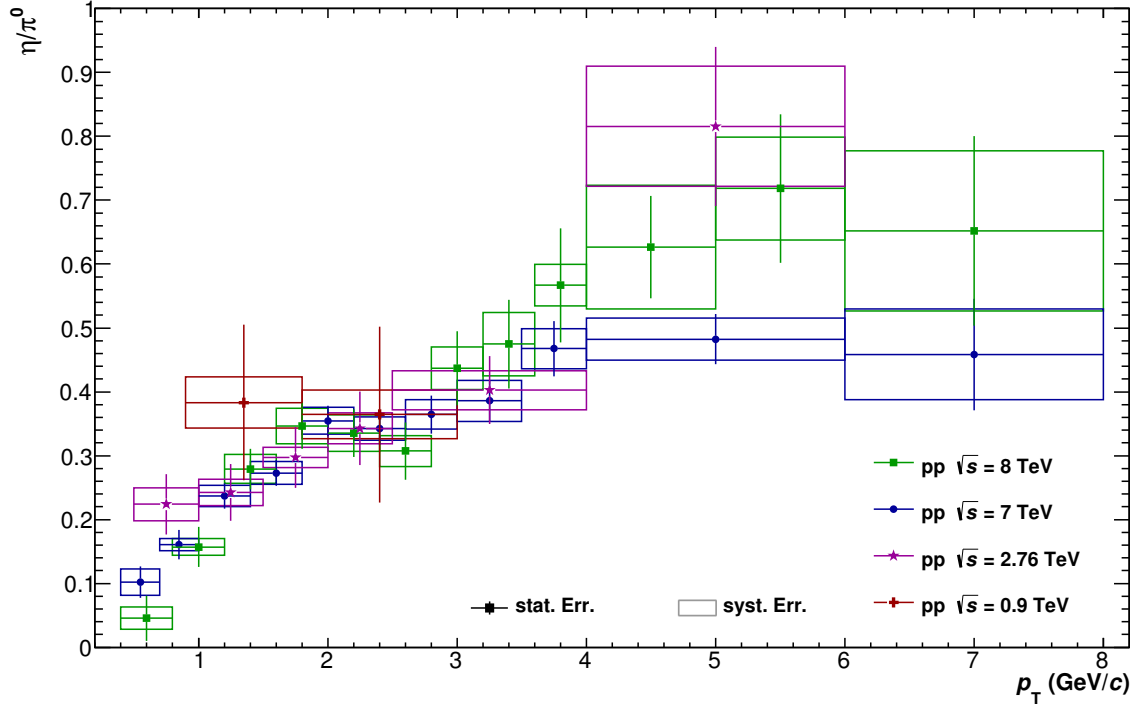


Figure 28: η/π^0 ratio for 900 GeV, 2.76 TeV, 7 TeV and 8 TeV. The ratio for 900 GeV and 7 TeV is taken from [2]

6 Conclusion and Outlook

In this thesis the Photon Conversion Method (PCM) is used to extract the differential invariant cross section of the η meson at $\sqrt{s} = 2.76$ and 8 TeV. The first bin of the 8 TeV cross section shows a deviation to both fitting functions but also a large statistical and systematic error. Here the problems of signal extraction in low transverse momentum can be seen. Furthermore the cross sections have been compared to NLO QCD calculations and it is found that there are similar deviations between the measured datapoints at 2.76 TeV and 8 TeV and theory calculations as found in the other two datasets at 0.9 TeV and 7 TeV.

After applying all corrections, which are done to the η spectra, to the π^0 and after subtracting secondary neutral pions, the η/π^0 ratio could be extracted. Here a deviation above $\sim 4 \text{ GeV}/c$ compared to the η/π^0 ratio at 7 TeV can be seen. This deviation could occur from an offset in the reweighted MC simulations and should be further investigated.

7 Appendix

7.1 Analyzed Runs

LHC11a

146746, 146747, 146748, 146801, 146802, 146803, 146804, 146805, 146806, 146807, 146817, 146824, 146856, 146858, 146859, 146860

LHC12a

176701, 176704, 176715, 176730, 176749, 176752, 176753, 176854, 176859, 176924, 176926, 176927, 176929, 177011, 177148, 177157, 177160, 177167, 177173, 177180, 177182

LHC12b

177580, 177592, 177597, 177612, 177620, 177624, 177671, 177798, 177799, 177804, 177858, 177860, 177861, 177864, 177869, 177942

LHC12c

179569, 179571, 179584, 179585, 179591, 179595, 179603, 179604, 179618, 179621, 179638, 179639, 179794, 179796, 179802, 179803, 179806, 179837, 179839, 179858, 179859, 179916, 179917, 179918, 179919, 179920, 180000, 180042, 180044, 180127, 180129, 180130, 180131, 180132, 180133, 180199, 180200, 180201, 180230, 180500, 180501, 180507, 180510, 180512, 180515, 180517, 180561, 180564, 180566, 180567, 180569, 180716, 180717, 180719, 180720, 181617, 181618, 181619, 181620, 181652, 181694, 181698, 181701, 181703, 182017, 182018, 182022, 182023, 182106, 182110, 182111, 182207, 182289, 182295, 182297, 182299, 182300, 182302, 182322, 182323, 182324, 182325, 182624, 182635, 182684, 182686, 182687, 182691, 182692, 182724, 182725, 182728, 182729, 182730, 182740, 182741, 182744

LHC12d

183913, 183916, 184127, 184131, 184132, 184135, 184137, 184138, 184183, 184188, 184208, 184209, 184210, 184215, 184216, 184371, 184673, 184678, 184682, 184687, 184784, 184786, 184928, 185029, 185031, 185116, 185126, 185127, 185132, 185133, 185134, 185157, 185160, 185164, 185189, 185196, 185198, 185203, 185206, 185208, 185217, 185221, 185282, 185284, 185288, 185289, 185291, 185292, 185293, 185296, 185299, 185300, 185302, 185303, 185348, 185349, 185350, 185351, 185356, 185359, 185360, 185361, 185362, 185363, 185371, 185375, 185378, 185459, 185460, 185461, 185465, 185474, 185574, 185575, 185578, 185580, 185581, 185582, 185583, 185588, 185589, 185659, 185687, 185695, 185697, 185698, 185699, 185701, 185738, 185764, 185765, 185768, 185775, 185776, 185778, 185784, 186073, 186163, 186164, 186165, 186167, 186205, 186208, 186319, 186320

LHC12f

186668, 186688, 186689, 186690, 186692, 186694, 186811, 186813, 186814, 186815, 186816, 186843, 186844, 186845, 186851, 186853, 186855, 186857, 186859, 186937, 186938, 186939, 186966, 186967, 186969, 186990, 186992, 186994, 187143, 187145, 187146, 187147, 187148, 187149, 187150, 187151, 187152, 187202, 187203, 187340, 187341, 187343, 187487, 187488, 187489, 187510, 187536, 187537, 187560, 187561, 187562, 187623, 187624, 187627, 187633,

187656, 187698, 187739, 187749, 187753, 187783, 187785, 187791, 187796, 188093, 188101

LHC12g

188442, 188443, 188444, 188446, 188448, 188449, 188454, 188455, 188499, 188503

LHC12h

189122, 189146, 189147, 189228, 189229, 189231, 189306, 189310, 189350, 189351, 189352, 189353, 189400, 189407, 189409, 189410, 189411, 189412, 189577, 189578, 189602, 189603, 189605, 189610, 189611, 189612, 189616, 189621, 189623, 189648, 189650, 189654, 189656, 189658, 189659, 189696, 189697, 189698, 190150, 190212, 190213, 190214, 190215, 190216, 190240, 190303, 190305, 190307, 190337, 190338, 190340, 190341, 190342, 190344, 190345, 190386, 190388, 190389, 190390, 190392, 190393, 190416, 190417, 190418, 190419, 190421, 190422, 190424, 190425, 190898, 190903, 190904, 190905, 190968, 190970, 190975, 190979, 190983, 191129, 191227, 191229, 191230, 191231, 191232, 191234, 191242, 191244, 191245, 191247, 191248, 191450, 191451, 192004, 192072, 192073, 192095, 192128, 192136, 192140, 192141, 192172, 192177, 192194, 192197, 192199, 192200, 192201, 192202, 192205, 192246, 192344, 192347, 192348, 192349, 192415, 192417, 192453, 192461, 192468, 192471, 192492, 192499, 192505, 192510, 192731, 192732

LHC12i

192772, 192775, 192778, 192779, 192820, 192822, 192824, 193004, 193005, 193007, 193008, 193010, 193011, 193014, 193047, 193189, 193194, 193049, 193051, 193092, 193093, 193094, 193097, 193148, 193150, 193151, 193152, 193155, 193156, 193184, 193187, 193188, 193192

7.2 Electron Selection

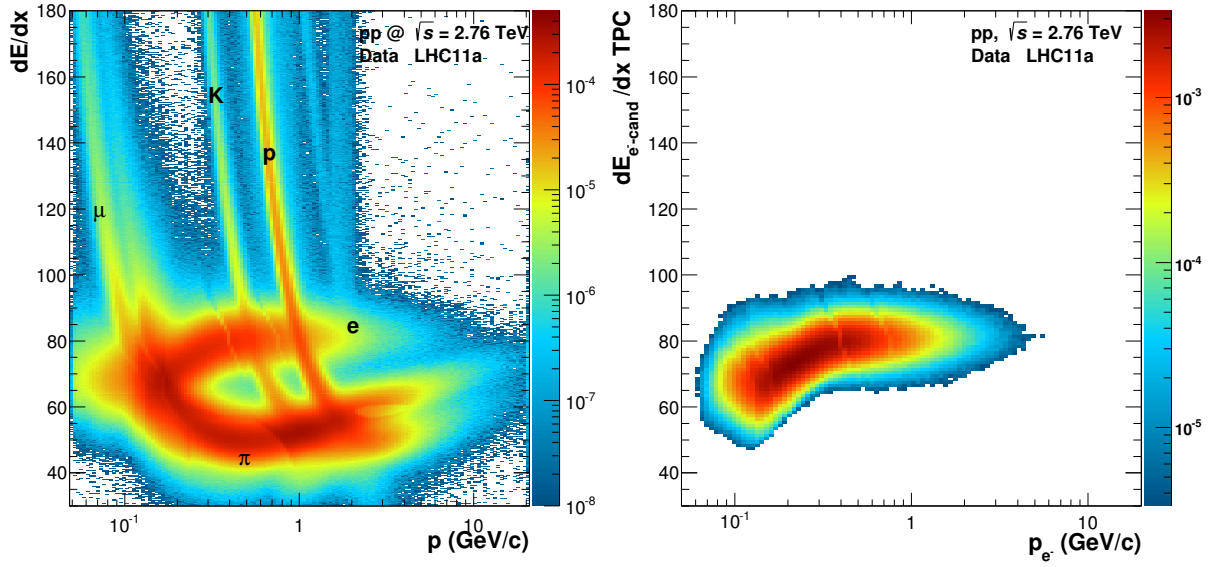


Figure 29: LHC11a: dE/dx distribution in the TPC before (left) and after (right) the electron PID cuts are applied.

7.3 Photon Selection

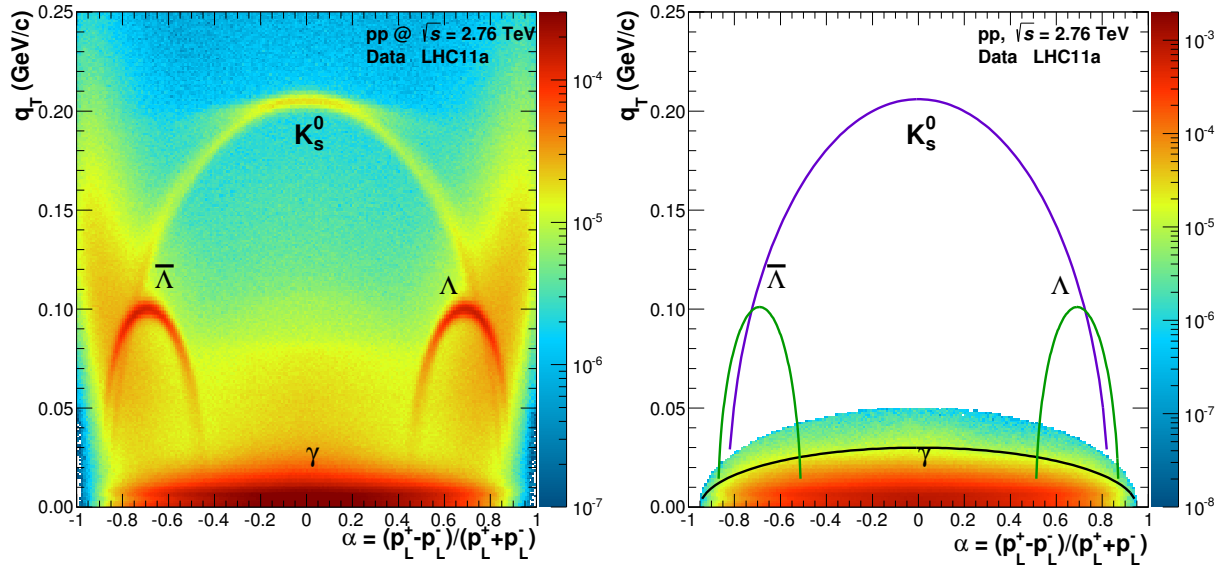


Figure 30: LHC11a: Armentos-Podolanski-Plot before cuts are applied (left) and after the photon cuts are applied (right)

7.4 Signal Extraction

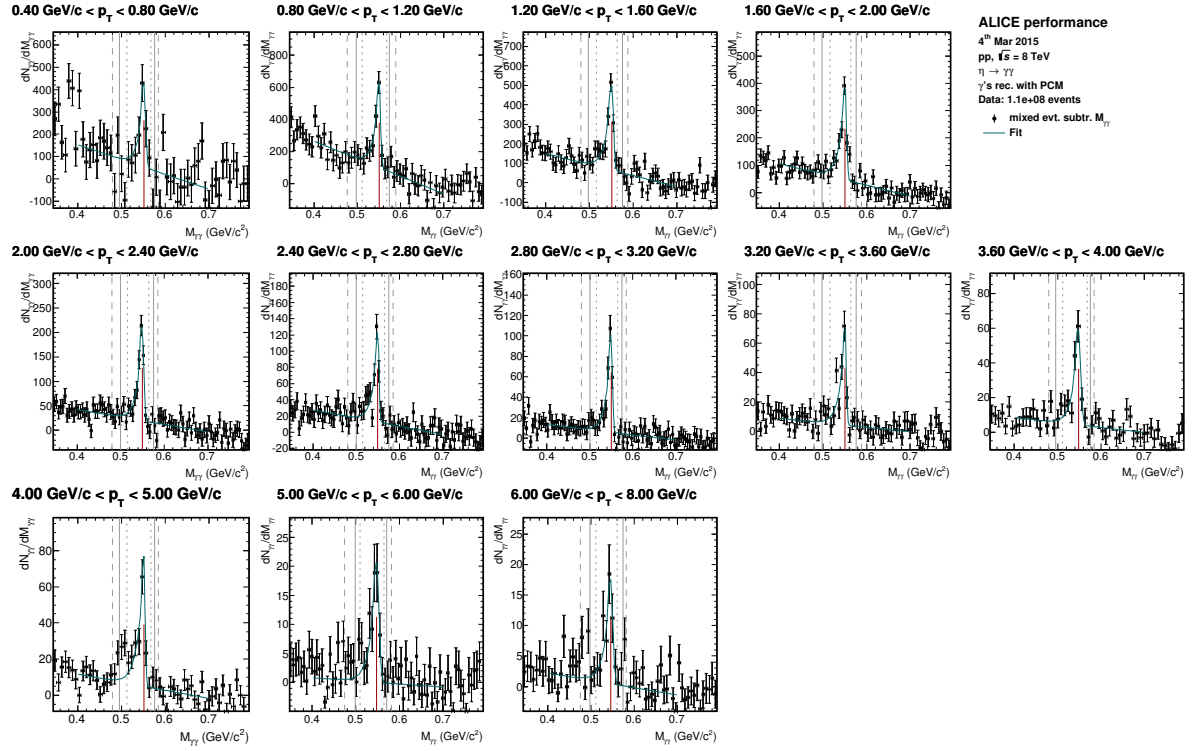


Figure 31: η meson signal extraction at $\sqrt{s} = 8$ TeV. The continuous gray line symbolizes the peak integration range used for this analysis. For the systematic error evaluation a narrower and wider integration range is used, which are represented by the dotted lines. The red line gives the peaks position which is equal to the meson's invariant mass in the respective transverse momentum p_T bin.

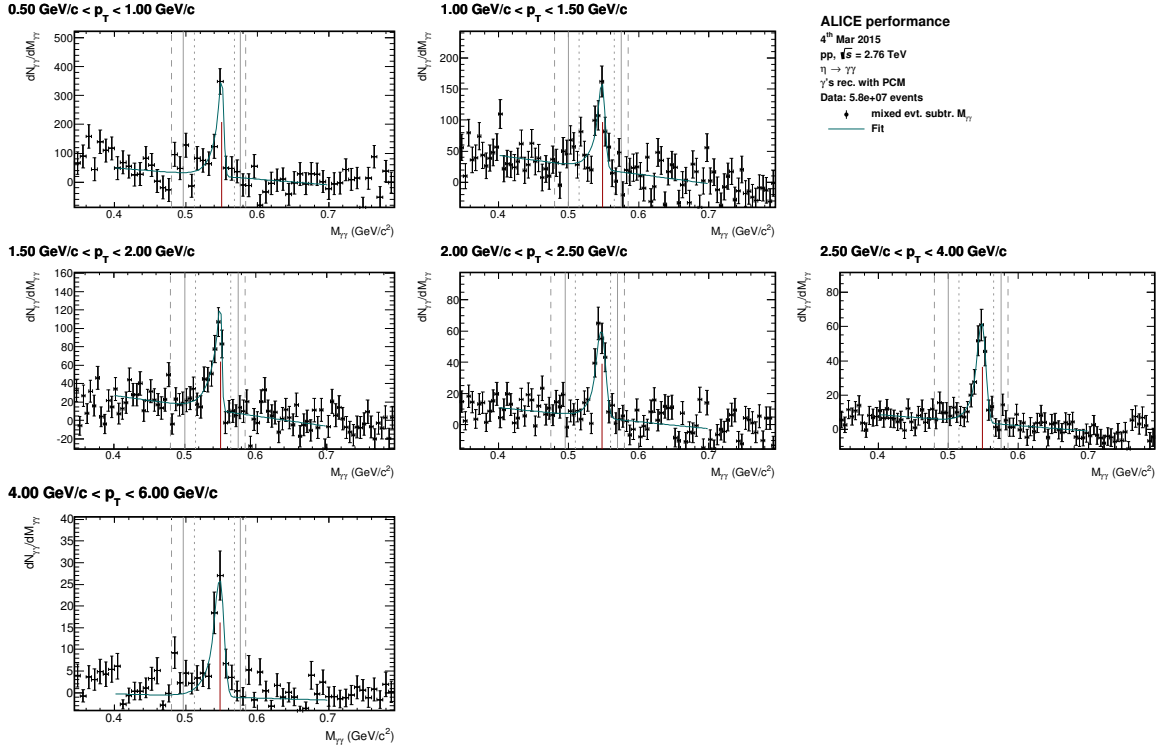


Figure 32: η meson signal extraction at $\sqrt{s} = 2.76$ TeV. The continuous gray line symbolizes the peak integration range used for this analysis. For the systematic error evaluation a narrower and wider integration range is used, which are represented by the dotted lines. The red line gives the peaks position which is equal to the meson's invariant mass in the respective transverse momentum p_T bin.

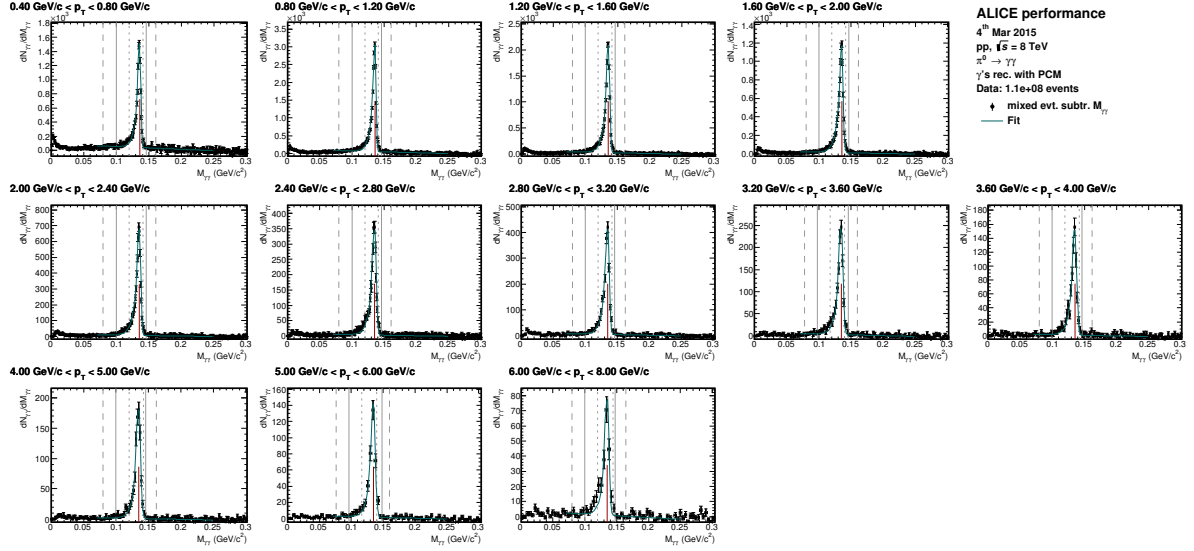


Figure 33: π^0 meson signal extraction at $\sqrt{s} = 8$ TeV in respective η meson binning. The continuous gray line symbolizes the peak integration range used for this analysis. For the systematic error evaluation a narrower and wider integration range is used, which are represented by the dotted lines. The red line gives the peaks position which is equal to the meson's invariant mass in the respective transverse momentum p_T bin.

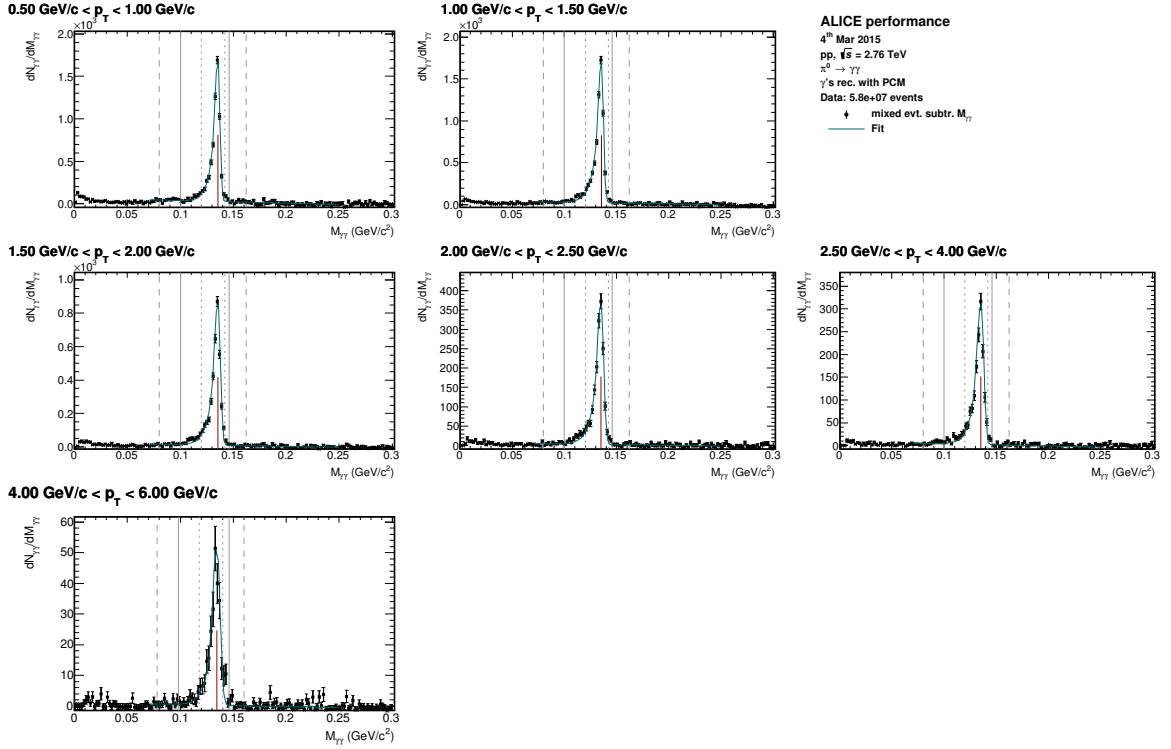


Figure 34: π^0 meson signal extraction at $\sqrt{s} = 2.76$ TeV in respective η meson binning. The continuous gray line symbolizes the peak integration range used for this analysis. For the systematic error evaluation a narrower and wider integration range is used, which are represented by the dotted lines. The red line gives the peaks position which is equal to the meson's invariant mass in the respective transverse momentum p_T bin.

7.5 DCA Bins

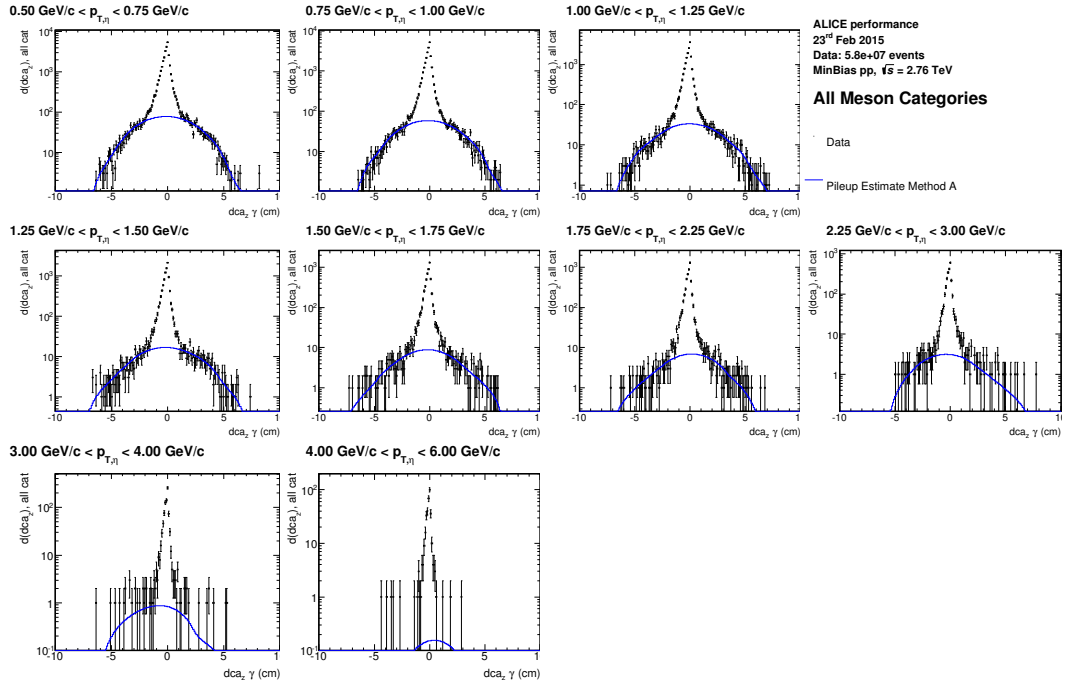


Figure 35: η meson DCA background estimation at $\sqrt{s} = 2.76$ TeV.

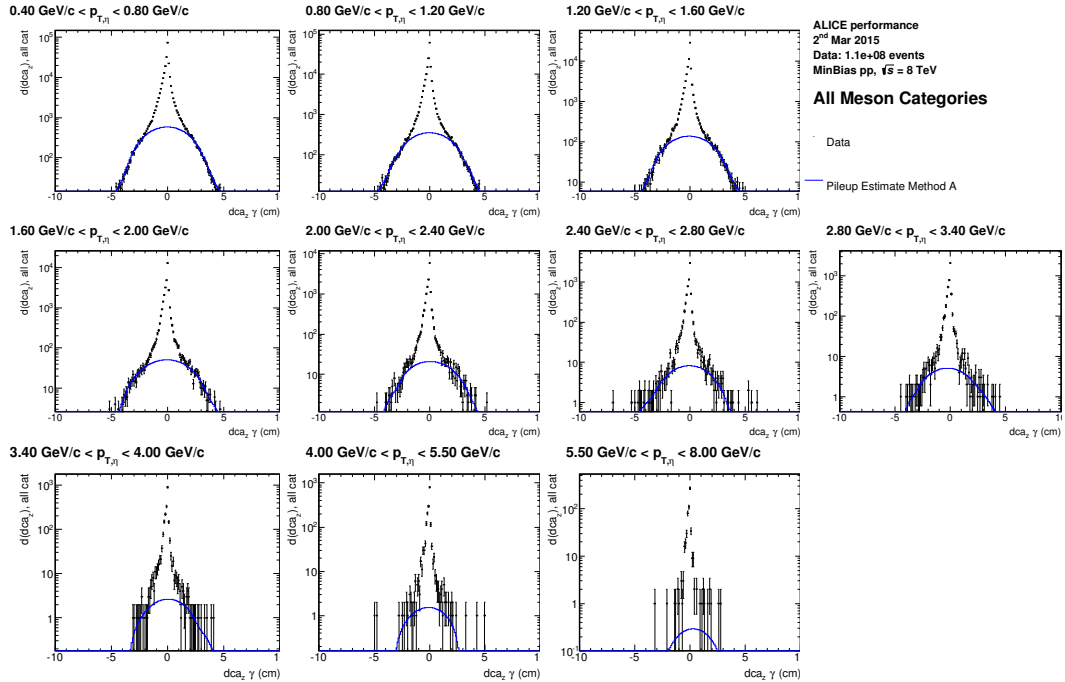


Figure 36: η meson DCA background estimation at $\sqrt{s} = 8$ TeV.

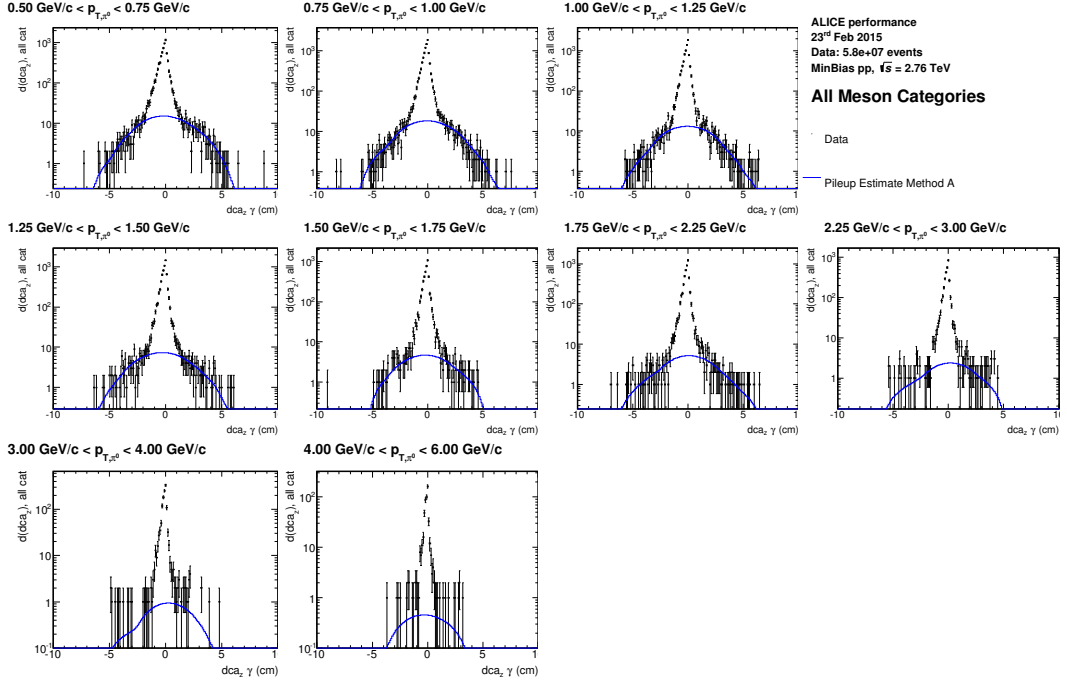


Figure 37: π^0 meson DCA background estimation at $\sqrt{s} = 2.76$ TeV in respective η meson binning.

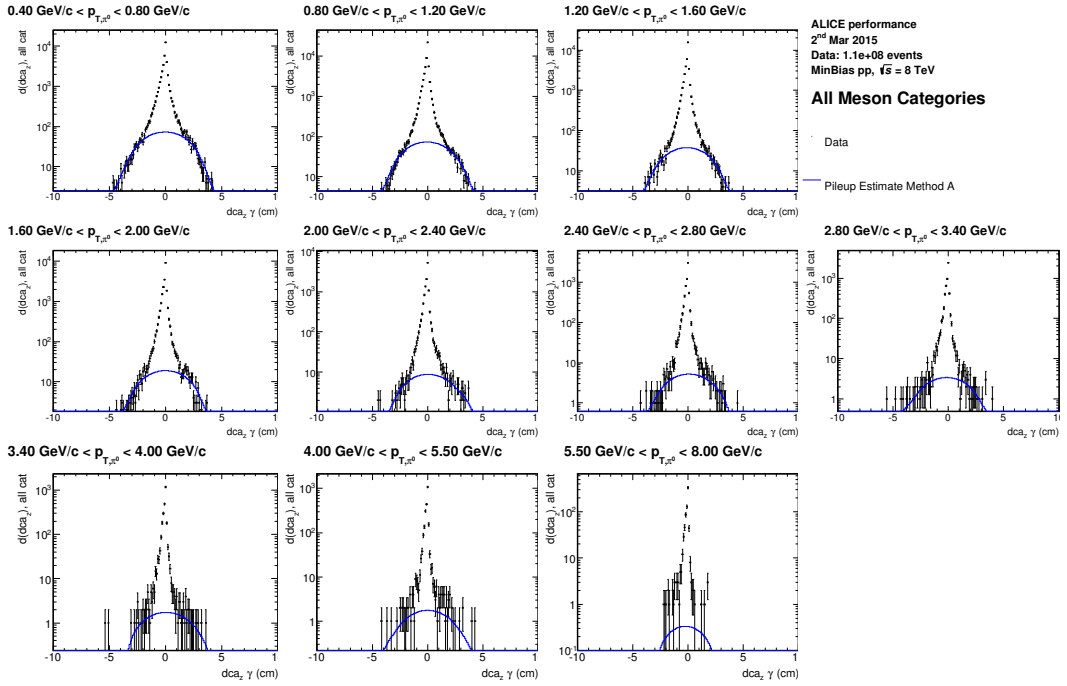


Figure 38: π^0 meson DCA background estimation at $\sqrt{s} = 8$ TeV in respective η meson binning.

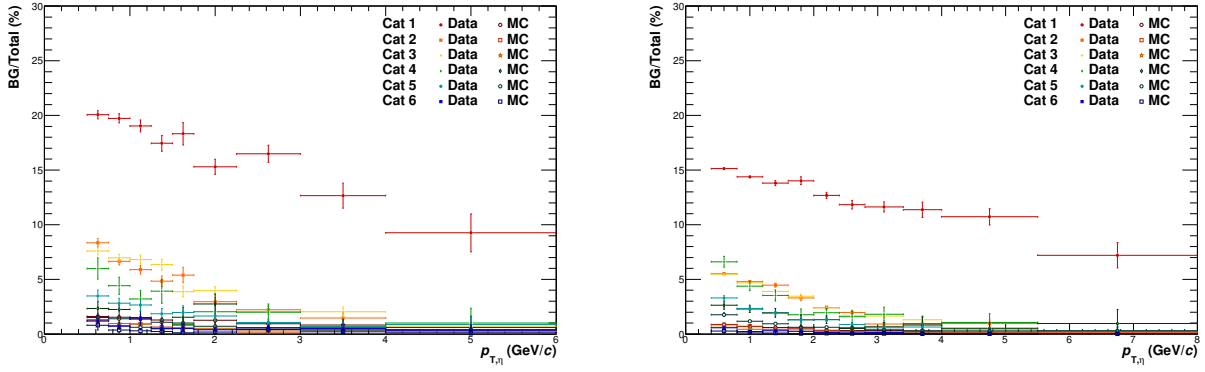


Figure 39: η meson pile up contribution divided into 6 meson categories for LHC11a(left) and LHC12[a-i](right)

7.6 Added Signals Weighting

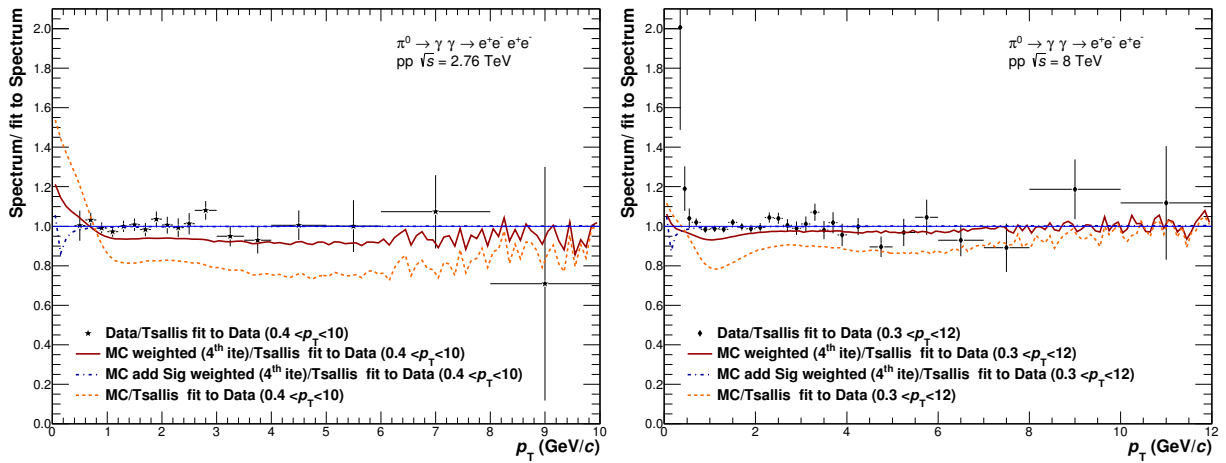


Figure 40: Ratio of weighted π^0 MC spectra with and without added signals to fit after the 4th iteration. LHC11a (left) and LHC12[a-i] (right). For the π^0 the reweighted MC do not deviate from a flat line within the statistical errors, so it can be used for efficiency calculations.

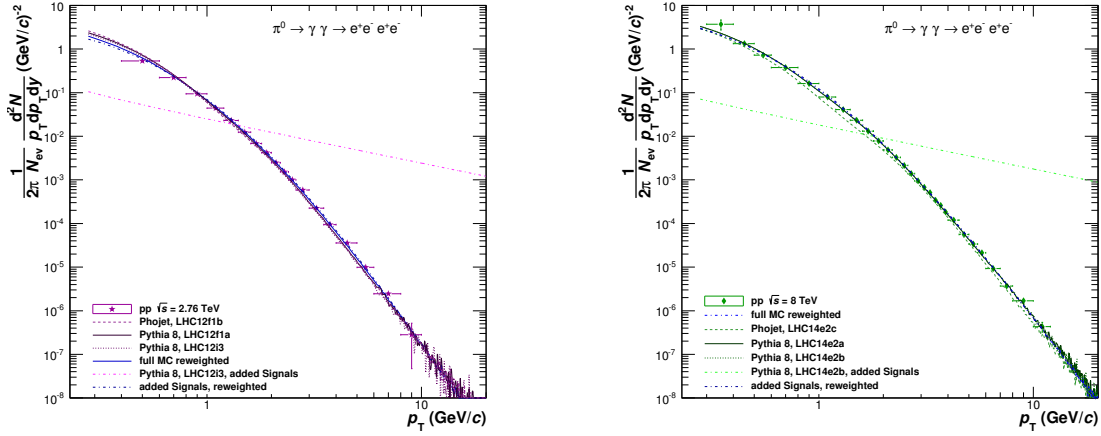


Figure 41: Comparison of minimum bias, weighted MC with and without added signals and unweighted MC added signals spectra for the π^0 meson for LHC11a (Left) and LHC12[a-i] (Right)

7.7 Systematic Error

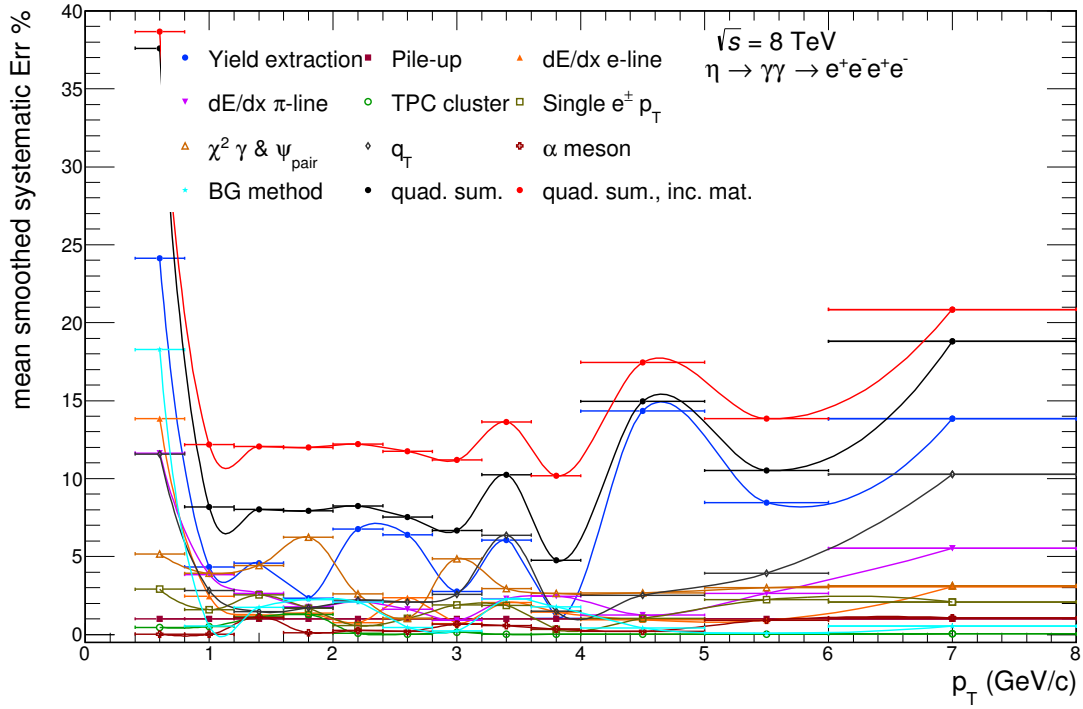


Figure 42: η meson systematic error sources at $\sqrt{s} = 8$ TeV.

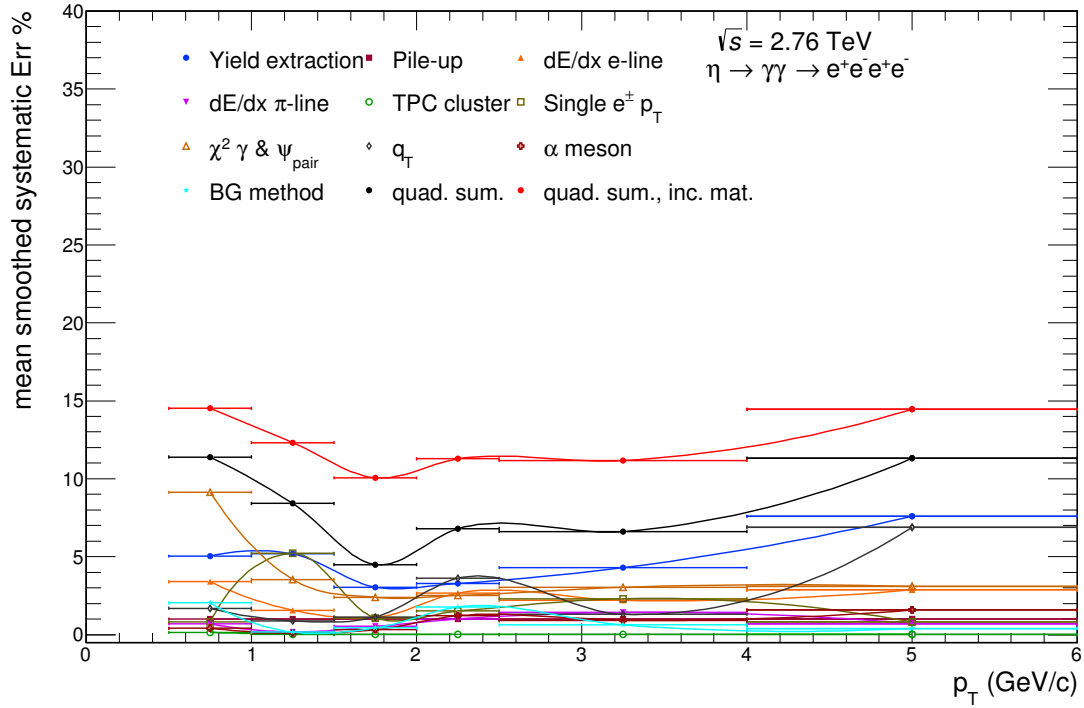


Figure 43: η meson systematic error sources at $\sqrt{s} = 2.76$ TeV.

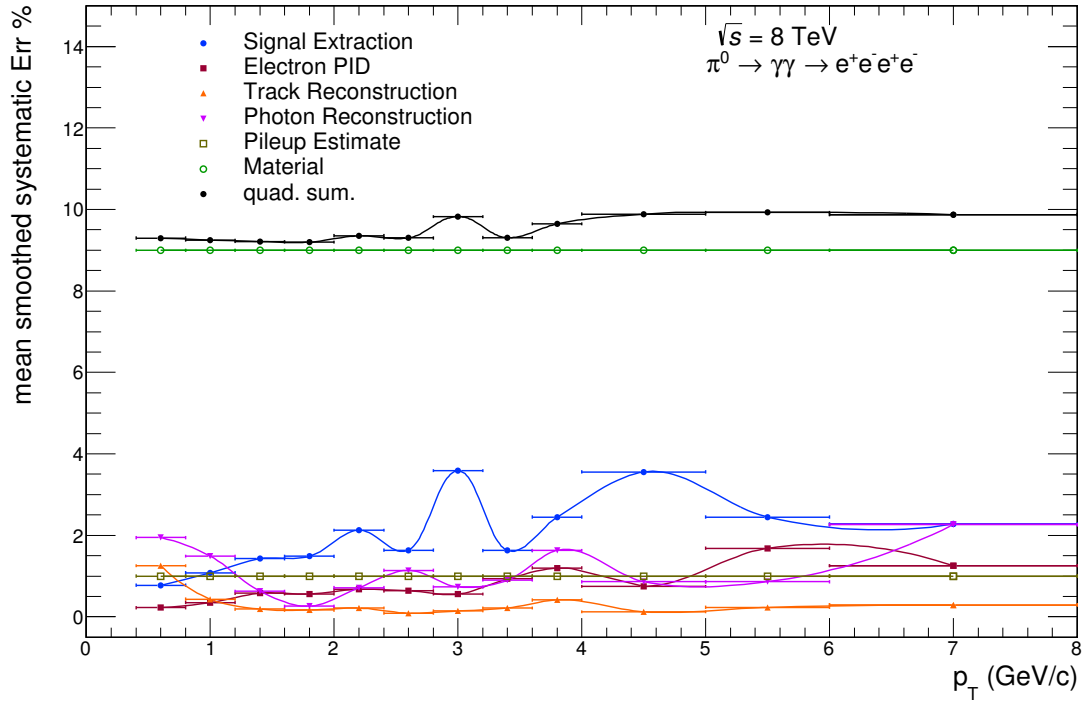


Figure 44: π^0 meson systematic error evaluation per category at $\sqrt{s} = 8$ TeV in respective η meson binning.

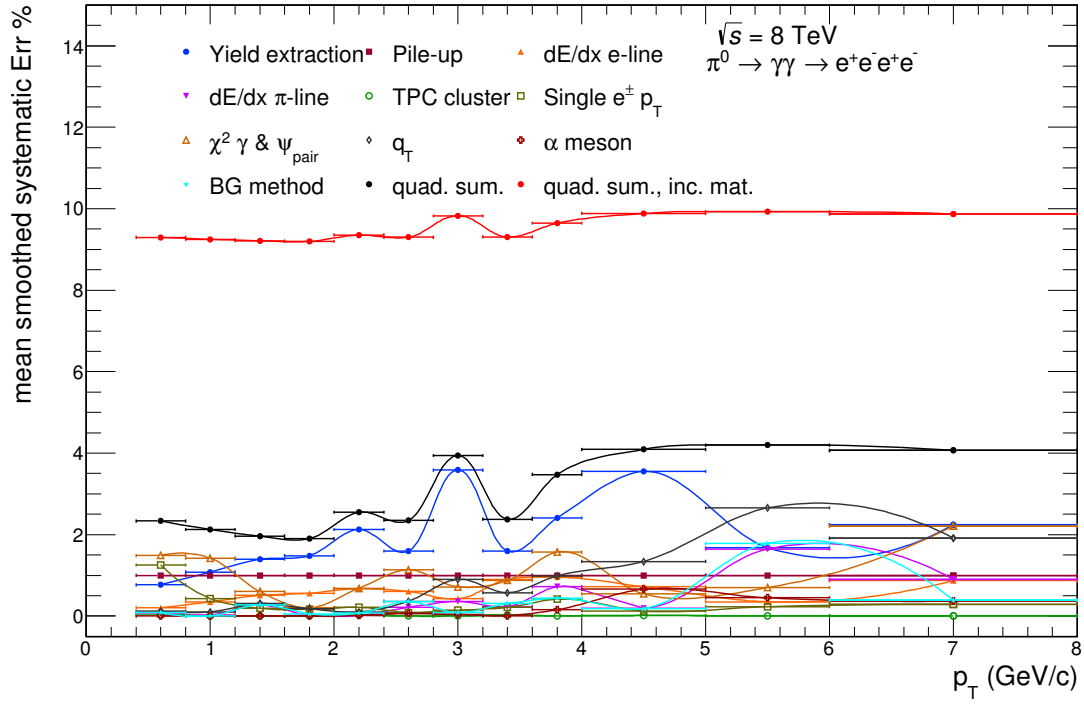


Figure 45: π^0 meson systematic error sources at $\sqrt{s} = 8$ TeV in respective η meson binning.

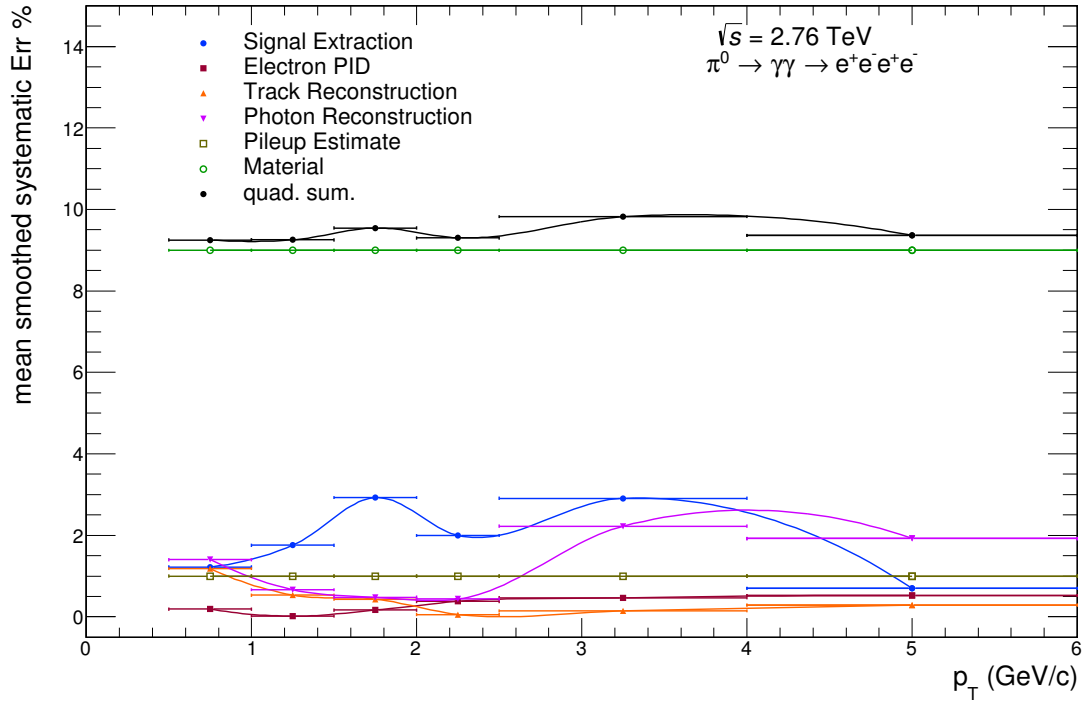


Figure 46: π^0 meson systematic error evaluation per category at $\sqrt{s} = 2.76$ TeV in respective η meson binning.

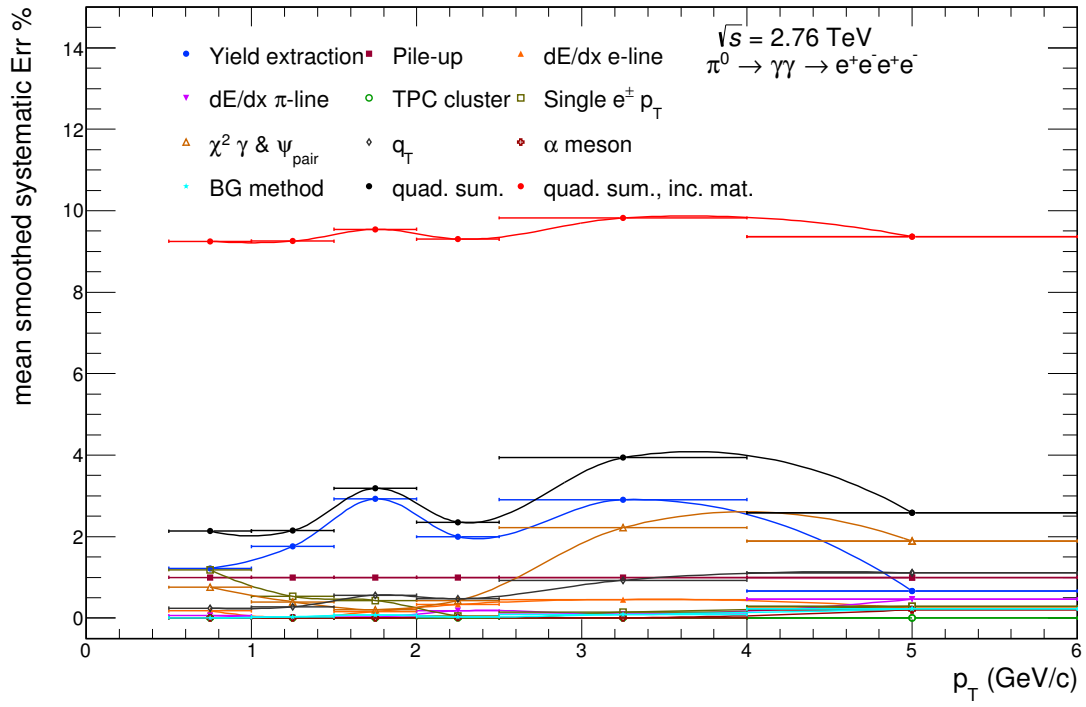


Figure 47: π^0 meson systematic error sources at $\sqrt{s} = 2.76 \text{ TeV}$ in respective η meson binning.

8 Acronyms and Technical Terms

AGS	Alternating Gradient Synchrotron
ALICE	A Large Ion Collider Experiment
ATLAS	A Toroidal LHC Apparatus
BR	branching ratio
CERN	European Organization for Nuclear Research
CMS	Compact Muon Solenoid
CTP	Central Trigger Processor
DCA	distance of closest approach
DPM	Dual Parton Model
EMCal	Electromagnetic Calorimeter
HMPID	High Momentum Particle Identification Detector
IROC	Inner Readout Chamber
ITS	Inner Tracking System
L0	level-0
L1	level-1
L2	level-2
LEIR	Low Energy Ion Ring
LHC	Large Hadron Collider
LHCb	LHC beauty
LINAC2	linear accelerator
LINAC3	linear accelerator
MC	Monte Carlo
MRPC	Multigap Resistive Plate Chamber
MTR	Muon Trigger
MWPC	multi-wire-proportional chamber
OROC	Outer Readout Chamber
PDF	parton distribution function

PHOS	Photon Spectrometer
PCM	Photon Conversion Method
PID	particle identification
pQCD	perturbative QCD
PS	Proton Synchrotron
PSB	Proton Synchrotron Booster
QCD	Quantum Chromodynamics
QGP	Quark-Gluon Plasma
RHIC	Relativistic Heavy Ion Collider
SDD	Silicon Drift Detector
SM	Standard Model
SPD	Silicon Pixel Detector
SPS	Super Proton Synchrotron
SSD	Silicon Strip Detector
TOF	Time-Of-Flight detector
TPC	Time Projection Chamber
TRD	Transition Radiation Detector
VZERO	VZERO
ZDC	Zero Degree Calorimeter

References

- [1] Georges Aad et al. “Observation of a new particle in the search for the Standard Model Higgs boson with the ATLAS detector at the LHC”. *Phys.Lett.* B716 (2012), pp. 1–29. DOI: 10.1016/j.physletb.2012.08.020. arXiv: 1207.7214 [hep-ex].
- [2] B. Abelev et al. “Neutral pion and η meson production in proton-proton collisions at $\sqrt{s} = 0.9$ TeV and $\sqrt{s} = 7$ TeV”. *Phys.Lett.* B717 (2012), pp. 162–172. DOI: 10.1016/j.physletb.2012.09.015. arXiv: 1205.5724 [hep-ex].
- [3] Betty Bezverkhny Abelev et al. “Performance of the ALICE Experiment at the CERN LHC”. *Int.J.Mod.Phys.* A29 (2014), p. 1430044. DOI: 10.1142/S0217751X14300440. arXiv: 1402.4476 [nucl-ex].
- [4] U. Abeysekara et al. “ALICE EMCAL Physics Performance Report” (2010). arXiv: 1008.0413 [physics.ins-det].
- [5] A. Akindinov et al. “Performance of the ALICE Time-Of-Flight detector at the LHC”. English. *The European Physical Journal Plus* 128.4, 44 (2013). DOI: 10.1140/epjp/i2013-13044-x. URL: <http://dx.doi.org/10.1140/epjp/i2013-13044-x>.
- [6] B. Alessandro et al. “ALICE: Physics performance report, volume II”. *Journal of Physics G: Nuclear and Particle Physics* 32 (2006), pp. 1295–2040.
- [7] *ALICE webpage*. URL: <http://aliceinfo.cern.ch/>.
- [8] *AliRoot webpage*. 2015. URL: <http://aliweb.cern.ch/Offline/>.
- [9] J. Alme et al. “The ALICE TPC, a large 3-dimensional tracking device with fast readout for ultra-high multiplicity events”. *Nucl.Instrum.Meth.* A622 (2010), pp. 316–367. DOI: 10.1016/j.nima.2010.04.042. arXiv: 1001.1950 [physics.ins-det].
- [10] INR RAS Artem Konevskikh. “T0 and V0 cross section from VdM scan, fill 3316” (2013). URL: <https://indico.cern.ch/event/276276/contribution/3/material/slides/0.pdf>.
- [11] Rene Bellwied. “Hadron formation in the deconfined matter at RHIC and LHC”. *PoS BORMIO2012* (2012), p. 045. arXiv: 1205.3625 [hep-ph].
- [12] F. Bock. “Neutral Pion and Eta Meson Production in pp and Pb–Pb Collisions at the LHC with the ALICE Detector”. MA thesis. University Heidelberg, 2012. URL: <http://www.physi.uni-heidelberg.de/Publications/Bock-Masterthesis.pdf>.
- [13] F. Bock et al. “Neutral meson measurements with conversions in ALICE in pp and Pb–Pb collisions at $\sqrt{s_{NN}} = 2.76$ TeV”. 2014. URL: <https://aliceinfo.cern.ch/Notes/node/217>.
- [14] Peter Braun-Munzinger and Johanna Stachel. “The quest for the quark-gluon plasma”. *Nature* 448 (2007), pp. 302–309. DOI: 10.1038/nature06080.
- [15] *CERN webpage*. 2015. URL: <http://home.web.cern.ch/>.
- [16] Serguei Chatrchyan et al. “Observation of a new boson at a mass of 125 GeV with the CMS experiment at the LHC”. *Phys.Lett.* B716 (2012), pp. 30–61. DOI: 10.1016/j.physletb.2012.08.021. arXiv: 1207.7235 [hep-ex].

- [17] Torsten Dahms. “Measurement of photons via conversion pairs in $s(\text{NN})^{1/2} = 200\text{-GeV}$ Au+Au collisions with the PHENIX experiment at RHIC”. *Eur.Phys.J. C*49 (2007), pp. 249–253. DOI: 10.1140/epjc/s10052-006-0089-2. arXiv: nucl-ex/0608009 [nucl-ex].
- [18] R. Engel. “PHOJET manual”. *University of Siegen preprint* (1995), pp. 95–05.
- [19] Abelev et al. *Technical Design Report for the Upgrade of the ALICE Inner Tracking System*. Tech. rep. CERN-LHCC-2013-024. ALICE-TDR-017. Geneva: CERN, 2013.
- [20] Fabrizio Ferro, Andrei Sobol, and Jean-Paul Guillaud. “Simulation of diffractive and non-diffractive processes at the LHC energy with the PHYTHIA and PHOJET MC event generators” (2004).
- [21] R.J. Fries and Berndt Muller. “Heavy ions at LHC: Theoretical issues”. *Eur.Phys.J. C*34 (2004), S279–S285. DOI: 10.1140/epjcd/s2004-04-026-6. arXiv: nucl-th/0307043 [nucl-th].
- [22] *Geant 4 webpage*. 2015. URL: <http://geant4.web.cern.ch/geant4/>.
- [23] David Griffiths. *Introduction to Elementary Particles*. 2nd. Wiley-VCH, 2008. DOI: 10.1002/9783527618460.
- [24] Claus Grupen and Boris Shwartz. *Particle Detectors*. Second. Cambridge Books Online. Cambridge University Press, 2008. ISBN: 9780511534966. URL: <http://dx.doi.org/10.1017/CB09780511534966>.
- [25] K. Nakamura et al. “Review of particle physics”. *J.Phys.* G37 (2010), p. 075021. DOI: 10.1088/0954-3899/37/7A/075021.
- [26] K.A. Olive et al (Particle Data Group). “Review of Particle Physics”. *Chin.Phys.* C38 (2014), p. 090001. DOI: 10.1088/1674-1137/38/9/090001.
- [27] *Phojet webpage*. 2015. URL: <http://www-ik.fzk.de/~engel/phojet.html>.
- [28] *Pythia 8 webpage*. 2015. URL: <http://home.thep.lu.se/~torbjorn/Pythia.html>.
- [29] *Root webpage*. URL: <http://root.cern.ch/>.
- [30] N. Schmidt. *Neutral Pion Measurements with Conversions in ALICE in pp Collisions at $\sqrt{s} = 8\text{ TeV}$* . 2014. URL: <http://http://www.physi.uni-heidelberg.de/Publications/Bachelorarbeit.pdf>.
- [31] Claus-Peter Schulz Ingolf V. Hertel. *Atoms, Molecules and Optical Physics 1*. Springer, 2015, pp. 46–48. DOI: 10.1007/978-3-642-54322-7.
- [32] Torbjorn Sjostrand, Stephen Mrenna, and Peter Z. Skands. “A Brief Introduction to PYTHIA 8.1”. *Comput.Phys.Commun.* 178 (2008), pp. 852–867. DOI: 10.1016/j.cpc.2008.01.036. arXiv: 0710.3820 [hep-ph].
- [33] C. Tsallis. “Possible Generalization of Boltzmann-Gibbs Statistics”. *J.Statist.Phys.* 52 (1988), pp. 479–487. DOI: 10.1007/BF01016429.
- [34] B.G. Zakharov. “Parton energy loss in the mini quark-gluon plasma and jet quenching in proton-proton collisions”. *J.Phys.* G41 (2014), p. 075008. DOI: 10.1088/0954-3899/41/7/075008. arXiv: 1311.1159 [hep-ph].
- [35] D.C. Zhou. “PHOS, the ALICE-PHOton Spectrometer”. *J.Phys.* G34 (2007), S719–S723. DOI: 10.1088/0954-3899/34/8/S81.

Acknowledgements

First of all I would like to thank Prof. Dr. Johanna Stachel for welcoming me in her friendly working group and for her useful comments and advices relating my analysis, which I received in the Photon Meetings.

Then I would like to thank my supervisor PD Dr. Klaus Reygers for giving me the opportunity to become part of the ALICE experiment and supporting me through my bachelor thesis.

My gratitude also goes to PD Dr. Kai Schweda for evaluating my thesis.

Special thanks to Friederike Bock and Lucia Leardini for guiding me through my analysis, answering all my questions and proof reading my thesis.

Furthermore I would like to thank Dr. Ana Marin and everybody from the Photon Conversion Group, who supported my work and gave me new inspirations when I needed them.

Last but not least I would like to thank my parents Sabine and Patrik and my whole family and friends for supporting me.

Erklärung

Ich versichere, dass ich diese Arbeit selbstständig verfasst und keine anderen als die angegebenen Quellen und Hilfsmittel benutzt habe.

Heidelberg, den 25.03.2015,

Alexander Koch